

1 **iPSC modeling shows uncompensated mitochondrial mediated oxidative stress underlies**
2 **early heart failure in hypoplastic left heart syndrome**

3
4
5 Xinxiu Xu¹, Kang Jin^{7,8}, Abha S. Bais¹, Wenjuan Zhu⁹, Hisato Yagi¹, Timothy N Feinstein¹, Phong
6 Nguyen¹⁰, Joseph Criscione¹⁰, Xiaoqin Liu¹, Gisela Beutner¹⁴, Kalyani B. Karunakaran¹⁵, Phillip
7 Adams⁶, Catherine K. Kuo^{10,11,12}, Dennis Kostka¹, Gloria S. Pryhuber¹³, Sruti Shiva^{3,4},
8 Madhavi K. Ganapathiraju⁵, George A. Porter Jr¹⁴,
9 Jiuann-Huey Ivy Lin^{1,2}, Bruce Aronow^{7,8}, Cecilia W. Lo^{1,*}

10
11 ¹Department of Developmental Biology,² Department of Critical Care Medicine,³Department of
12 Pharmacology and Chemical Biology,⁴Vascular Medicine Institute,⁵Department of Biomedical
13 Informatics,⁶Department of Anesthesiology, University of Pittsburgh, Pittsburgh, PA, USA

14 ⁷University of Cincinnati, Cincinnati, United States

15 ⁸Biomedical Informatics, Cincinnati Children's Hospital Research Foundation, Cincinnati, USA

16 ⁹Centre for Cardiovascular Genomics and Medicine, Faculty of Medicine,
17 The Chinese University of Hong Kong, Hong Kong, China

18 ¹⁰Department of Biomedical Engineering, University of Rochester, Rochester, NY, USA

19 ¹¹Fischell Department of Bioengineering, University of Maryland, College Park, MD

20 ¹²Department of Orthopaedics, University of Maryland School of Medicine, Baltimore, MD

21 ¹³Department of Pediatrics, Pediatrics and Environmental Medicine

22 ¹⁴Pediatrics, Pharmacology and Physiology, and Aab Cardiovascular Research Institute
23 University of Rochester Medical Center, Rochester, NY, USA.

24 ¹⁵Supercomputer Education and Research Centre, Indian Institute of Science, Bangalore, India.

25
26
27
28
29

30 * Corresponding author. Email: cel36@pitt.edu. Phone: 412-427-9319.

31 **Summary**

32 Hypoplastic left heart syndrome (HLHS) is a severe congenital heart defect with 30%
33 mortality from heart failure (HF) in the first year of life, but why only some patients suffer early-
34 HF and its cause remain unknown. Modeling using induced pluripotent stem cell-derived
35 cardiomyocytes (iPSC-CM) showed early-HF patient iPSC-CM have increased apoptosis, redox
36 stress, and failed antioxidant response. This was associated with mitochondrial permeability
37 transition pore (mPTP) opening, mitochondrial hyperfusion and respiration defects. Whereas
38 iPSC-CM from patients without early-HF had hyper-elevated antioxidant response with increased
39 mitochondrial fission and mitophagy. Single cell transcriptomics showed dichotomization by HF
40 outcome, with mitochondrial dysfunction and endoplasmic reticulum (ER) stress associated with
41 early-HF. Importantly, oxidative stress and apoptosis associated with early HF were rescued by
42 sildenafil inhibition of mPTP opening or TUDCA suppression of ER stress. Together these
43 findings demonstrate a new paradigm for modeling clinical outcome in iPSC-CM, demonstrating
44 uncompensated mitochondrial oxidative stress underlies early HF in HLHS.

45

46 **Keywords**

47 heart failure, Hypoplastic left heart syndrome (HLHS), congenital heart disease (CHD), induced
48 pluripotent stem cell derived cardiomyocytes (iPSC-CM), permeability transition pore (mPTP),
49 endoplasmic reticulum (ER).

50 **Introduction**

51 Congenital heart disease is one of the most common birth defects affecting 0.5% of live
52 births (Feinstein et al., 2012). Hypoplastic left heart syndrome (HLHS) is a severe CHD in which
53 the left ventricle (LV) and aorta are small and nonfunctional. While survival with HLHS is made
54 possible by staged surgical palliation that recruits the RV to become the single pumping chamber
55 (Oster et al., 2013), there remains high morbidity and mortality. The 10-year transplant free
56 survival stands at only 39-50% (Driscoll et al., 1992; Garcia et al., 2020; Gentles et al., 1997).
57 However, the greatest risk is in the first year of life with 30% mortality reported (Alsoufi et al.,
58 2016; Cleves et al., 2003; Tweddell et al., 2002). While HLHS patients have complicated clinical
59 course, the early mortality is largely associated with ventricular dysfunction with rapid progression
60 to acute heart failure (HF) (Garcia *et al.*, 2020). Unfortunately, therapies developed for HF in
61 adults have been ineffective for treating HF in HLHS (Hsu et al., 2010; Shaddy et al., 2007).
62 Without insights into the underlying mechanisms driving early HF in HLHS, the clinical
63 management of this patient population is largely empirical.

64 Investigations into the mechanism of HLHS-HF have been hampered by the difficulty in
65 obtaining human heart tissue for analysis. An alternative strategy entails in vitro disease modeling
66 using induced pluripotent stem cells (iPSC) and their differentiated derivatives such as
67 cardiomyocytes (iPSC-CM), endothelial/endocardial cells, and other cell types. While this has
68 been successfully deployed for investigating HLHS disease mechanisms (Gaber et al., 2013;
69 Hrstka et al., 2017; Jiang et al., 2014a; Kobayashi et al., 2014; Miao et al., 2020; Paige et al., 2020),
70 no studies have explored the possibility of using iPSC-CM to model disease outcome. Particularly
71 compelling is the question as to why only some HLHS patients develop early-HF even with the
72 same surgical palliation, and what might be the underlying cause for HF. The feasibility to model

73 HLHS HF in iPSC-CM is suggested by our previous studies of a mouse model of HLHS (Liu et
74 al., 2017). We found cell autonomous defects were associated with prenatal/neonatal lethality from
75 HF in the HLHS mutant mice. In the present study, we showed mouse iPSC-CM generated from
76 the HLHS mice replicated defects observed in the HLHS mouse heart tissue, confirming the
77 defects are cell autonomous and thus suitable for in vitro iPSC-CM modeling. Generating iPSC
78 and iPSC-CM from HLHS patients dichotomized by clinical outcome, either with or without acute
79 early-HF (Xinxu Xu, 2018), we further investigated and demonstrated the feasibility of using
80 patient iPSC-CM to investigate HF outcome in vitro. These studies provided surprising insights
81 not only into possible causes for early HF in HLHS, but they also uncovered mechanisms that may
82 protect against early HF in HLHS patients surviving heart transplant free.

83 RESULTS

84 Cell Autonomous Mitochondrial defects in the Ohia HLHS Mouse Model

85 The Ohia HLHS mouse model exhibits mid to late gestation lethality with acute heart failure
86 characterized by severe pericardial effusion with poor cardiac contractility, this is associated with
87 decreased proliferation and increased apoptosis (Liu *et al.*, 2017). Ultrastructural analysis showed
88 the myocardium with poorly organized thin myofilaments and altered mitochondrial morphology
89 (Liu *et al.*, 2017). Dynamic changes in mitochondria morphology play an important role in the
90 developmentally regulated metabolic switch from glycolysis to oxidative phosphorylation, a
91 process that also plays a critical role in regulating cardiomyocyte differentiation (Hom *et al.*, 2011).
92 This entails closure of the mitochondrial permeability transition pore (mPTP) and formation of a
93 mitochondrial transmembrane potential ($\Delta\Psi_m$) mediating oxidative phosphorylation. Using
94 primary cardiomyocyte explants from the E14.5 *Ohia* HLHS mouse heart, we measured the $\Delta\Psi_m$,
95 in cardiomyocytes from the right and left ventricle (RV, LV). A reduction was observed in both
96 the RV and LV cardiomyocytes, indicating failure of the mPTP to close (**Figure 1A**). However,
97 mitochondrial mass was unchanged (**Extended Data Figure S1A**).

98 To determine whether the abnormal open state of the mPTP is a cell autonomous defect, we
99 generated iPSC from *Ohia* mutant fibroblasts and differentiated them into iPSC-CM (**Figure 1B**).
100 These *Ohia* iPSC-CM generated entirely *in vitro* showed reduced cell proliferation with lower
101 *Myh6/Myh7* ratio indicating a cardiomyocyte differentiation defect (**Figure 1C,D;Figure S1C,D**),
102 phenotypes reminiscent of those observed in the *Ohia* HLHS myocardium. Poor cardiac function
103 was also indicated by reduced beat frequency (**Figure 1E**). Mitochondrial function was assessed
104 with measurement of $\Delta\Psi_m$ and oxygen consumption rate (OCR) using the Seahorse Flux Analyzer
105 (**Figure 1F,G**). This analysis uncovered mPTP and mitochondrial respiration defects in both the

106 undifferentiated *Ohia* iPSC and iPSC-CM. While the iPSC showed lower respiratory reserve and
107 respiratory maxima (**Figure S1B**), the iPSC-CM from *Ohia* exhibited reduction in basal respiration,
108 ATP production, respiratory reserve, and respiratory maxima (**Figure 1G; Figure S1E**). Together
109 these findings indicate the mitochondrial dysfunction, and proliferation and differentiation defects
110 observed in the *Ohia* HLHS heart tissue are cell autonomous.

111 **Generating HLHS Patient iPSC-CM for Investigating Early Heart Failure**

112 The finding that *Ohia* iPSC-CM replicated defects seen in the HLHS heart tissue suggested
113 HLHS patient derived iPSC-CM may have utility for investigating acute early HF in HLHS
114 patients. For this study, we generated iPSC from 10 HLHS patients, including six >5-year old with
115 transplant free survival (Group I) (**Figure 1H; Figure S2A**), and four that died (n=3) or survived
116 (n=1) with a heart transplant at <1 year of age (Group II). In addition, we also generated iPSC
117 from 3 healthy subjects as controls. Using standard iPSC-CM differentiation protocols, iPSC-CM
118 at Day 16-20 of differentiation were generated and used for the subsequent analysis.

119 **Impaired Cardiomyocyte Differentiation and Contractile Dysfunction**

120 The iPSC-CM were found to be predominantly ventricle-like as shown by high expression of
121 the ventricular marker MYL2, but low expression of atrial marker NR2F2 (Biendarra-Tiegs et al.,
122 2019) (**Figure 1I**). The Group II iPSC-CM had fewer cardiac troponin T (cTnT) positive cells with
123 higher ratio of *MYH6* (atrial myosin heavy chain) to *MYH7* (ventricular myosin heavy chain)
124 transcripts, indicating poor differentiation (Jiang et al., 2014b) (**Figure S2E; Figure 1J**). Group II
125 iPSC-CM also showed reduced Ki67, but increased pH3 immunostaining, suggesting cell cycle
126 disturbance with possible metaphase arrest (**Figure 1K; Figure S2F,G**), reminiscent of findings in
127 the *Ohia* HLHS LV (Liu *et al.*, 2017). Poor cardiomyocyte differentiation was indicated by low
128 expression of cTnT (A-band) and α -actinin (Z-disc) containing myofilaments together with

129 increased myofibrillar disarray (**Figure 1L, M**). However, no change was observed for
130 cardiomyocyte cell size (**Figure S2H**).

131 Further assessment of cardiomyocyte contractile function showed the Group II iPSC-CM have
132 lower beat frequency with reduced calcium transients (**Figure 1N-P;Supplemental Video 1&2**).
133 Examination of the profile of calcium transients confirmed the majority (84~89%) of the iPSC-
134 CM are ventricle-like (Cyganek et al., 2018) (**Figure S2I**). Analysis of the cardiomyocyte
135 contractile motion by high resolution video microscopy showed reduced fractional shortening
136 accompanied by decreased contraction and relaxation rates in the Group II but not Group I iPSC-
137 CM. This was associated with reduction in the diastolic sarcomere length, but not systolic
138 sarcomere length (**Figure 1Q-S;Figure S2J,K; Supplemental video 3**). Together these findings
139 indicate the Group II iPSC-CM have profound differentiation defects causing impaired calcium
140 handling and poor contractile function.

141 **Mitochondrial Respiration and Transition Pore Closure Defects**

142 Various parameters of mitochondrial function were assessed in the iPSC-CM. A marked
143 decrease in mitochondrial membrane potential ($\Delta\Psi_m$) was observed in the Group II iPSC-CM,
144 suggesting abnormal mPTP opening (**Figure 2A**). OCR measurements showed mitochondrial
145 respiration defects with reduction in basal respiration, ATP production, H⁺ leak, respiratory
146 reserve and maximal respiratory capacity (**Figure 2B**). For Group I iPSC-CM, only respiratory
147 reserve and maximal respiratory capacity showed significant change (**Figure 2B**). These same two
148 parameters also were reduced in the undifferentiated iPSC of Group II patients, findings
149 reminiscent of the *Ohia* mouse iPSC (**Figure S2C & S1B**). Western blotting showed no change in
150 abundance of the electron transport chain (ETC) complexes (**Figure S3A,B**).

151 Consistent with the uncoupling of oxidative phosphorylation in the Group II iPSC-CM, we

152 observed a marked increase in mitochondrial reactive oxygen species (ROS) indicated by
153 increased MitoSOX staining (**Figure 2C**) (Hom *et al.*, 2011). Also observed was a reduction in
154 nitric oxide (NO), suggesting perturbation of protein nitrosylation required for normal
155 mitochondrial respiration (**Figure S3F**). The mitochondrial respiration defects and increase in
156 ROS in the Group II iPSC-CM are accompanied by increase in apoptosis and activation of a DNA
157 damage response, findings similar to those observed in *Ohia* (Liu *et al.*, 2017) and human HLHS
158 fetal heart tissue (Gaber *et al.*, 2013) (**Figure 2D-F**). Parallel analysis of the Group I iPSC-CM
159 showed no significant change in these parameters.

160 **Perturbation of Mitochondrial Dynamics**

161 As the regulation of mitochondrial fission and fusion play important roles in metabolic and
162 redox regulation, its disturbance can contribute to cardiomyocyte death in HF (Marin-Garcia and
163 Akhmedov, 2016). Using confocal imaging, we assessed mitochondrial mass and morphology. In
164 the Group II but not Group I iPSC-CM, mitochondrial linkage constant and cluster length were
165 increased, while mitochondrial mass was unchanged, indicating increase in mitochondrial fusion
166 in the Group II iPSC-CM (**Figure 2F,G; Figure S3C-E**). Group II iPSC-CM also showed
167 decreased expression of *DNML (DRP1)*, gene regulating mitochondrial fission, and increase in
168 *MFN1*, gene promoting mitochondrial fusion (**Figure 2H**). Expression of *BNIP3/NIX* regulating
169 mitophagy were decreased in Group II but increased in Group I iPSC-CM (**Figure 2H**). Lysosomes,
170 which are involved in mitophagy, were reduced in both Group I and II (**Figure 2I**). These findings
171 indicate the hyperfused mitochondria in the Group II iPSC-CM likely arise from altered
172 mitochondrial dynamics associated with increased mitochondrial fusion and decreased mitophagy.
173 In contrast, Group I iPSC-CM exhibited more normal mitochondrial dynamics that may be
174 accompanied by increase in mitophagy.

175 **Mitochondrial Respiration Defects in the Left Ventricle of HLHS Human Heart Tissue**

176 To explore the clinical relevance of the abnormal mitochondrial function observed in the
177 HLHS patient derived iPSC-CM, heart tissue was obtained from HLHS patients undergoing heart
178 transplant. Analysis of mitochondrial respiration showed basal respiration was reduced in the
179 HLHS-LV vs. RV tissue, but such LV-RV difference was not observed in heart tissue from age-
180 matched heart transplant patient with doxorubicin induced HF (**Figure 2J**). Analysis of two
181 additional HLHS neonates and two neonatal control subjects the HLHS-LV being more sensitive
182 to lower ADP, indicating possible adaptation to bioenergetic stress. However, respiration in the
183 LV failed to increase with increasing ADP concentration, indicating the hypoplastic LV has
184 reduced respiratory capacity (Ventura-Clapier et al., 2011) (**Figure 2K;Figure S3G**). Western
185 blotting showed no change in ETC components (**Figure S3H,I**). These findings suggest LV
186 specific mitochondrial respiration defects in HLHS.

187 **Defects in Yap-Regulated Antioxidant Response**

188 Activation of an antioxidant defense pathway occurs during developmental with metabolic
189 transition to mitochondrial respiration (Perrelli et al., 2011; Tsutsui et al., 2011). This pathway is
190 regulated by transcription factors NRF2 (Itoh et al., 1999) together with PITX2 and YAP (Tao et
191 al., 2016). These three transcription factors play an essential role in regulating the expression of
192 antioxidant genes that scavenges ROS to prevent oxidative stress. These transcription factors also
193 have critical roles in regulating cardiac regeneration and repair, with YAP also shown to regulate
194 heart organ size (Heallen et al., 2013; von Gise et al., 2012; Zhou et al., 2015). Interestingly, YAP
195 also has been demonstrated to regulate mitochondrial fission (Huang et al., 2018).

196 We observed *NRF2* and *PITX2* transcripts are both reduced in Group II iPSC-CM, but in
197 Group I iPSC-CM, *PITX2* was elevated and *NRF2* was unchanged (**Figure 3A**). In contrast, *YAP1*

198 transcripts showed no change in either Group or Group II iPSC-CM (data not shown). Analysis of
199 downstream genes in the antioxidant pathway revealed up regulation of thioredoxin (*TXN*),
200 peroxiredoxin 1 (*PRDX1*), glutathione peroxidase 1 (*GPX1*), and superoxide dismutase 2 (*SOD2*)
201 in the Group I iPSC-CM, but in Group II, expression was either unchanged or downregulated, such
202 as for *PRDX1* (**Figure 3A**). In the Group I iPSC-CM, we also observed increased expression of
203 HIF1 α , a transcription factor regulating cell stress response to hypoxia. This was associated with
204 increased expression of *VEGF*, a known downstream transcriptional target of HIF1 α (**Figure 3A**)
205 (Guimaraes-Camboa et al., 2015).

206 Antibody staining showed nuclear localization of NRF2/PITX2/YAP were reduced in the
207 Group II iPSC-CM, while in Group I, only PITX2 showed a modest reduction in comparison to
208 Group II and control (**Figure 3B-D; Figure S3J**). However, total YAP and β -catenin protein
209 expression levels were unchanged (**Figure S3K,L**). We further examined expression of
210 downstream target genes of YAP - *NRG1* and *MYC* (*Artap et al., 2018*), and observed both were
211 reduced in the Group II iPSC-CM. In contrast, the opposite was observed in Group I with *NRG1*
212 being upregulated, while *MYC* was unchanged (**Figure 3F**). However, nuclear localized β -catenin
213 and transcripts for two downstream YAP/ β -catenin targets, *BIRC5* and *SNAI2*, were reduced in
214 both Groups I and II iPSC-CM (**Figure 3E,F**). Together these findings show defects in the
215 mounting of an effective antioxidant response in the Group II iPSC-CM (**Figure 3G**). In contrast,
216 in Group I, the antioxidant capacity is expanded, and may promote and support the restoration of
217 redox homeostasis.

218 **Inhibition of mPTP Opening Rescues Mitochondrial Respiration and Apoptosis**

219 The mPTP closure defect observed in the Group II iPSC-CM suggests compounds promoting
220 mPTP closure might rescue the mitochondrial defect. This was investigated using the Seahorse

221 Analyzer to screen compounds known to inhibit mPTP opening(Martel et al., 2012) or otherwise
222 modulate mitochondrial respiration. This analysis yielded 7 compounds showing some rescue of
223 mitochondrial respiration in the Group II iPSC-CM. This included fasudil, sildenafil, cyclosporin
224 A (CsA), Metformin, JP4, SS31, and Y27632 (**Figure S4A**). In contrast, treatment with ascorbic
225 acid, a general antioxidant, had no effect (Myung et al., 2013; Ye et al., 2013). Given sildenafil is
226 commonly used among CHD patients for its vasodilatory effects(Galie et al., 2005), more in-depth
227 analysis was carried out with sildenafil (**Figure 4**).

228 Titration of sildenafil showed rescue down to 0.1 μM , which restored not only $\Delta\Psi_m$ and
229 maximal mitochondrial respiration. This also reduced mitochondrial ROS to levels similar to the
230 Group I and control iPSC-CM (**Figure 4A-C; Figure S4B-D**). Sildenafil is also known to affect
231 NO production, but normal NO level was restored only at 1.0 μM concentration (**Figure**
232 **S4D**)(Prabhu et al., 2013). Cell proliferation, apoptosis (**Figure 4E,F**), and YAP nuclear
233 trafficking were rescued at ten times lower dose of 0.01 μM (**Figure 4G**). However, β -catenin
234 nuclear trafficking was not rescued (**Figure 4H; Figure S4E**). To verify that sildenafil is targeting
235 the mPTP, we further assessed treatment with BKA (bongkrelic acid) and CAT
236 (carboxyatractyloside), which activate and inhibit the mPTP, respectively. As expected, BKA but
237 not CAT rescued the mPTP defect, with opposing effects observed for maximal and basal OCR,
238 mitochondrial ROS, and YAP nuclear localization (**Figure 4I-L, Figure S4F**). Similar treatment
239 of control iPSC-CM showed repression of respiration by CAT, while BKA had no effect (**Figure**
240 **S4G**).

241 **Single Cell Transcriptome Profiling**

242 We performed single cell RNAseq on iPSC-CM from two Group II patients, 7042 with heart
243 transplant at 11 months and patient 7052 deceased at 2 months, Group I patient 7464 surviving

244 transplant free at 7 years of age, and healthy control subject 1053. Data was obtained from 4403
245 cardiomyocytes forming 9 clusters (Stuart et al., 2019) (**Figures 5A and S5A-C**). Marker gene
246 analysis showed these cardiomyocytes were largely of ventricular identity (**Figure S5D**). Clusters
247 0 (CM I), 1 (CM II) and 5 (CM III) comprising the majority of cells are well differentiated
248 cardiomyocytes of increasing maturation (**Figure S5E; Supplemental Spreadsheet 2**). Group II
249 vs. control comparison yielded the greatest number of DEGs (**Figure 5B**). Enrichment was
250 observed for mitochondrial related pathways in all three clusters, suggesting Group II
251 mitochondrial defects likely arise early in cardiomyocyte differentiation (**Figure 5C**). In contrast,
252 Group I vs Control yielded the fewest DEGS. These were associated with heart development and
253 muscle organ development terms in Clusters 0 and 1, and mitochondrial related terms in Cluster 5
254 (**Figure 5E**). Group II vs. Group I comparisons yielded apoptosis and cell death in Clusters 0 and
255 1, (**Figure 5D**), and tRNA modification and noncoding RNA in Cluster 5.

256 Combining DEGs from all pairwise comparisons showed the number of DEGs increased
257 with disease severity (**Figure 5F**). Only control 1053 yielded terms related to muscle and muscle
258 contraction. Group I 7464 recovered protein translation and cell cycle, and Group II 7042 yielded
259 mitochondria and mitochondrial translation. In Group II 7052, hypoxia related pathways were
260 recovered, but mitochondrial related terms were also recovered in DEGs shared with 7042 (**Figure**
261 **5F; Spreadsheet 2**). Overall, a high percentage of the DEGs were found to be mitochondrial
262 related (**Figure 5G**). Heatmap generated comprising only the mitochondrial related DEGS was
263 nearly identical to that for all DEGs (**Figure 5H vs. F**), indicating genes with the highest fold
264 change are mostly mitochondrial related. Interestingly pathways related to mitochondrial
265 translation, elongation, and termination were recovered in both 7464 (Group I) and 7042 (Group
266 II), but with only 60 DEGs in 7464, vs. 183 DEGs in 7042 (**Figure 5H;Spreadhseet 2**). Differing

267 from 7042, mitochondrial DEGs in 7052 were hypoxia related, confirming the recovery of these
268 same pathways in all DEG analysis (**Figure 5F**). In mitochondrial DEGs shared between
269 7042/7052 shared, the recovery of ATP synthesis and oxidative phosphorylation were observed,
270 suggesting bioenergetic deficits associated with Group II patients.

271 DEG analysis based on Group II vs. Group I comparison yielded further evidence of the
272 effective dichotomization of HLHS patients into two functional groups (**Figure 5I**). Profiling
273 upregulated DEGs showed the two Group II patients are similar to each other, while Group I is
274 similar to control (**Figure 5I**). This analysis also recovered 28 genes highly expressed only in
275 patient 7052 (see region denoted by asterisk in **Figure 5I**) - 14 are related to mitochondria, hypoxia
276 and/or cell death, including EGLN3 encoding prolyl hydroxylase, an oxygen sensor that promotes
277 HIF1 α degradation (**Figure 5J;Supplemental Spreadsheet 2**). Assembly of a protein interactome
278 network incorporating 26 of these genes showed pathway enrichment for hypoxia, apoptosis, and
279 oxidative stress, indicating these genes are part of a functional network contributing to early HF
280 in patient 7052 (**Figure S6;Supplemental Spreadsheet 2**).

281 **Molecular Chaperone Rescues Mitochondrial Respiration and Apoptosis**

282 Recovery of ER stress and UPR in Cluster 7 from the scRNAseq analysis was notable (**Figure**
283 **6A**), given ER stress can be triggered by mitochondrial dysfunction and oxidative stress. and ER
284 stress has been associated with HF (Schiattarella et al., 2019). This pathway has not been
285 investigated previously in the context of HLHS. Real time PCR analysis confirmed elevated
286 expression of genes (*XBPI, ATF4, ATF6*) associated with the three conserved ER stress pathways
287 (**Figure 6B**). All three pathways were elevated in patient 7052, and two (*ATF4 ATF6*) were
288 elevated in 7042. In contrast, Group I patient 7464 showed no change relative to control (**Figure**
289 **6B**). Similar analysis of three downstream ER stress target genes *HSPA5, DDIT3, and DNAJC3*

290 showed all three were upregulated in 7052, but only *DDIT3* and *DNJC3* were elevated in 7042. In
291 contrast, all three genes were down regulated in Group I patient 7464 (**Figure 6B**). We noted these
292 same cell stress related genes were also up regulated in the *Ohia* HLHS heart tissue, consistent
293 with their severe HF phenotype (Liu *et al.*, 2017). To assess the potential functional impact of UPR
294 on the HLHS iPSC-CM, we treated the iPSC-CM with Tauroursodeoxycholic acid (TUDCA), a
295 molecular chaperone known to promote protein folding and suppress ER-stress. TUDCA treatment
296 promoted mPTP closure, reduced mitochondrial ROS, and rescued NO production in the Group II
297 iPSC-CM (**Figure 6C-E**). TUDCA also rescued YAP nuclear translocation, restored
298 cardiomyocyte proliferation and blocked apoptosis (**Figure 6F-H**). These findings suggest ER
299 stress and UPR may contribute to the early HF in Group II patients.

300 **Enrichment of variants associated with mitochondrial metabolism**

301 Given HLHS is well described as having a genetic etiology, we further investigated the whole
302 exome sequencing data available for 6 of our 10 HLHS patients (Group II 7042, Group I
303 7131,7400,7438,7434,7464). High impact variants comprising unique loss-of-function variants
304 were recovered (**Figure S7A;Supplemental Spreadsheet 3**). Using Webgestalt/KEGG pathway
305 enrichment analysis, four genes were identified as significantly associated with metabolic
306 pathways (*OXAIL,NNMT,NEU3,ALDH7A1*) (**Supplemental Spreadsheet 3**). An protein-protein
307 interactome (PPI) was constructed using these four genes to explore connections to Hippo
308 signaling, a pathway that plays a critical role in regulating YAP degradation and nuclear
309 translocation (Meng *et al.*, 2016). The interactome showed enrichment for Hippo and Wnt
310 signaling, and also heart development and many mitochondrial-related terms, including regulation
311 of mitochondrial membrane permeability (**Fig7A,B;Supplemental Spreadsheet 3**).

312 Building on this finding, we interrogated the WES data from another 41 HLHS patients

313 comprising 19 patients who died or had heart transplant (unfavorable outcome) and 22 HLHS
314 patients surviving transplant-free beyond 5 years of age (favorable outcome). Interrogating for
315 unique loss-of-function variants or predicted damaging missense or splice variants yielded
316 159 genes from the unfavorable outcome group and 194 genes from the favorable group (**Figure**
317 **S7A;Supplemental Spreadsheet 3**). Rendering these genes in a network plot using Metascape
318 recovered terms such as “Ion channel transport”, “Mitochondrial gene expression”, and
319 “Mitochondrial translation” in association with genes from the unfavorable group, while “lipid
320 location, response to IL-17” were associated with the favorable group (**Figure 7C;Supplemental**
321 **Spreadsheet 3**). Some pathways were shared by both groups such as calcium signaling, MAPK
322 signaling, and nervous system development. Examining the genes recovered for intersection with
323 an expanded MitoCarta-related inventory of mitochondrial genes yielded 19 genes from the
324 unfavorable and 11 from favorable group (Calvo et al., 2012; Pagliarini et al., 2008)
325 (**Supplemental Spreadsheet 3**). ToppGene analysis of these overlapping genes recovered from
326 the unfavorable group yielded multiple mitochondrial related pathways, including mitochondrial
327 translation (**Figure 7D**). Most of these genes are highly expressed in cardiomyocytes of the human
328 fetal heart (Cui et al., 2019), supporting a role in HLHS pathogenesis (**Figure 7E**).

329 **DISCUSSION**

330 Our objective in this study was to investigate why only some HLHS patients suffer early-HF
331 and the possible cause of early-HF. Analysis of iPSC-CM from our HLHS mouse model and
332 HLHS patients revealed both have cell autonomous defects involving failure in mPTP closure.
333 Thus, mitochondrial defects seen in vivo in the HLHS mouse heart were replicated in the mouse
334 iPSC-CM. This was associated with defects in mitochondrial respiration and poor cardiomyocyte
335 differentiation. The mitochondrial defects observed in the mouse heart and iPSC-CM were
336 replicated in iPSC-CM of HLHS patients with early HF, suggesting a common cell autonomous
337 mechanism involving mitochondrial defects underlying early-HF in HLHS.

338 For these studies, we selected HLHS patients with extreme phenotype comprising death or
339 surviving with heart transplant at less than one year of age (Group II), as the first year of life poses
340 the greatest risk with 30% mortality reported (Oster *et al.*, 2013). For comparison, HLHS patients
341 surviving transplant free at more than 5 years of age were recruited (Group I). Using these two
342 HLHS group comparisons and control subjects, we interrogated a myriad of parameters such as
343 cardiomyocyte differentiation, myocyte contractility and calcium handling, mPTP closure,
344 mitochondrial dynamics, respiration, and regulation of the antioxidant pathway. From this
345 comprehensive analysis, we showed the iPSC-CM from the Group II patients closely resembled
346 each other, while the Group I patients were more similar to control. This was further corroborated
347 with scRNASeq analysis, which showed transcriptome profiles of the two Group II patients are
348 similar to each other, but very different from Group I patient 7464.

349 In the Group II iPSC-CM, we uncovered severe oxidative stress arising from
350 mitochondrial dysfunction. This is associated with mPTP closure defect with altered mitochondrial
351 dynamics and reduced mitophagy. When combined with a failed antioxidant response, this would

352 exacerbate the redox stress to enhance apoptosis and increase DNA damage. Also observed were
353 severe defects in cardiomyocyte differentiation with poor myocyte function. Cardiomyocyte
354 differentiation and maturation are known to be regulated by mPTP closure (Hom *et al.*, 2011) and
355 a metabolic switch to mitochondrial respiration (Mills *et al.*, 2017; Nakano *et al.*, 2017) . We note
356 skeletal myoblast differentiation is also regulated by a similar metabolic transition(Fortini *et al.*,
357 2016a). Moreover, this skeletal myoblast metabolic transition was shown to be modulated by
358 mitophagy(Fortini *et al.*, 2016b). Also observed in the Group II iPSC-CM is the up regulation of
359 ER stress pathways. This likely occurs secondary to the mitochondrial associated increase in ROS,
360 exacerbating the oxidative stress induced apoptosis. Recent studies have in fact shown an
361 important role for ER stress and UPR in HF (Schiattarella *et al.*, 2019). Of significant interest from
362 a therapeutic standpoint, apoptosis in the Group II iPSC-CM can be rescued using sildenafil (Ascah
363 *et al.*, 2011) to inhibit mPTP opening or TUDCA to suppress UPR. This was associated with the
364 reduction of mitochondrial ROS, recovery of mitochondrial respiration, and restoration of YAP
365 nuclear translocation. Together these findings support mitochondrial mediated oxidative stress as
366 underlying the acute early-HF in HLHS. The scRNAseq analysis further suggests this may involve
367 defects in the HIF1 α pathway, altered mitochondrial translation, and bioenergetic deficits, findings
368 that will need to be further investigated in future studies.

369 In contrast to Group II iPSC-CM, the Group I iPSC-CM show similarities to that of control
370 with near normal mitochondrial respiration and normal mitochondrial dynamics without oxidative
371 stress nor increase in apoptosis. Nevertheless, the Group I iPSC-CM have reduced mitochondrial
372 respiratory reserve and reduced maximal respiration, indicating an overall reduction in total
373 respiratory capacity. Importantly, nuclear localization of NRF2, YAP1, PITX2 was maintained,
374 albeit with some reduction observed for PITX2. This was associated with striking gene expression

375 changes that included elevated expression of many antioxidant genes, and the elevated expression
376 of HIF1 α and its downstream target genes. Genes regulating mitophagy were also elevated, while
377 *MFN1*, gene regulating mitochondrial fusion was down regulated. Significantly, key mediators of
378 all three ER stress pathways were downregulated. Together these findings suggest the maintenance
379 of mitochondrial dynamics in conjunction with the suppression of oxidative and ER stress by a
380 vigorous NRF2/YAP/PITX2 mediated antioxidant response may provide protection from early-
381 HF in Group I patients. As Group I iPSC-CM also showed better differentiation with improved
382 myocyte contractile function, these factors also may contribute to improved clinical outcome.

383 The WES sequencing analysis showed pathogenic variants in HLHS patients with
384 unfavorable outcome are enriched for genes in mitochondrial related pathways. While the genetic
385 causes for HLHS remains largely unknown, pathogenic variants in mitochondrial related pathways
386 may contribute to the pathogenesis of HLHS or they may act as genetic modifiers affecting clinical
387 outcome. It is worth noting *Sap130*, one of the two genes causing HLHS in the *Oha* mouse model
388 is known to regulate genes involved in mitochondrial metabolism via the Sin3A complex (Pile et
389 al., 2003), suggesting the developmental etiology of HLHS may involve the disturbance of
390 mitochondrial metabolism (Liu *et al.*, 2017). We note there is mounting evidence of the integral
391 role for metabolism and mitochondrial respiration in the regulation of a wide range of
392 developmental processes (Mills *et al.*, 2017).

393 In summary, our findings point to the common involvement of mitochondrial dysfunction
394 in HLHS regardless of HF outcomes. This is supported by another study that also reported
395 mitochondrial defects in HLHS iPSC-CM (Paige *et al.*, 2020). With the outcome-based iPSC-
396 modeling, we showed the mitochondrial dysfunction and oxidative stress underlie the early HF in
397 HLHS, while a hyper-elevated antioxidant response may provide protection from oxidative and

398 ER stress to prevent early HF. Together these findings suggest early HF is the result of
399 uncompensated mitochondrial mediated oxidative stress. The observed altered regulation of YAP1
400 suggests the tantalizing possibility that the mitochondrial defects also may contribute to the LV
401 hypoplasia in HLHS, a question that warrants further studies.

402 We also showed possible therapeutic intervention with the targeting of mPTP closure with
403 sildenafil or suppression of UPR with TUDCA. We note Sildenafil is already being used
404 empirically to treat HF associated with pulmonary hypertension(Guglin et al., 2016). Suppression
405 of UPR, such as with TUDCA, may be another therapeutic path. TUDCA is currently in clinical
406 trial for amyotrophic lateral sclerosis(Elia et al., 2016). Providing antioxidant might be another
407 therapeutic course, although we found ascorbic acid did not rescue mitochondrial defects in the
408 Group II iPSC-CM. Overall, our iPSC modeling has yielded new insights into the underlying
409 causes for early HF in HLHS and suggest new evidence-based therapies that will need to be further
410 investigated. These findings suggest a new paradigm for modeling clinical outcome using patient
411 stratified iPSC.

412 **Limitations of the Study**

413 One limitation of our study is the inclusion of iPSC-CM from only 10 patients. However,
414 this compares favorably to other studies that typically include iPSC from only one to three patients,
415 and no study had controlled for outcome(Gaber *et al.*, 2013; Hrstka *et al.*, 2017; Jiang *et al.*, 2014a;
416 Kobayashi *et al.*, 2014; Miao *et al.*, 2020; Paige *et al.*, 2020). Nevertheless, the generalizability of
417 our findings will require future confirmation with analysis of iPSC-CM from additional patients.
418 As our study was focused on acute early-HF in patients less than one year old, the relevance of
419 these findings to HF in older HLHS patients will require further studies. While additional factors
420 may contribute to HF in older patients, the involvement of mitochondrial dysfunction is likely.

- 421 This is suggested by the recovery of mitochondrial-related pathogenic variants in the expanded
422 WES analysis of 41 HLHS patients that included older patients with heart transplant.

423 **FIGURE LEGENDS**

424 **Figure 1. Mouse and human HLHS iPSC and iPSC-CM show differentiation and functional**
425 **defects.**

426 (A) Mitochondrial transmembrane potential ($\Delta\Psi_m$) was measured with TMRE/Mitotracker
427 Green in CM from E13.5 wildtype (WT) mouse embryo (n=3) left ventricle (WT-LV; n=124 CMs)
428 and right ventricle (RV; n=86 CMs), and E13.5 *Ohia* HLHS mutant (n=3), LV (n=105 CMs) and
429 RV (n=118 CMs)

430 (B) Mouse iPSC were generated from WT and HLHS mouse embryonic fibroblasts (two
431 independent lines each) and further differentiated into iPSC-CM.

432 (C) Ki67 quantification showed reduced proliferation of the HLHS (n=1800) vs. WT (n=2800)
433 iPSC-CM.

434 (D) *Myh6/Myh7* transcript ratio is decreased in the *Ohia* HLHS iPSC-CM vs. WT, indicating a
435 maturation defect. WT n=6, and HLHS n=5.

436 (E) Beat frequency of *Ohia* HLHS iPSC-CM (n=17 clusters quantified) was reduced
437 compared to WT (n=38 myocyte clusters quantified).

438 (F) The mitochondrial membrane potential ($\Delta\Psi_m$) was reduced in the mouse HLHS iPSC-CM
439 (n=43) compared to WT (n=56).

440 (G) Mitochondrial respiration parameters were obtained from Seahorse Analyzer oxygen
441 consumption rate (OCR) measurements (n=3 independent experiments).

442 (H) Human iPSC-CM were generated from HLHS patients and controls. Group I comprises
443 patients with transplant free survival >5 years old. Group II are patients who died or survived with

444 heart within one year of age. Controls are healthy subjects without disease. Functional assessments
445 were conducted on 18-22 days of iPSC-CM differentiation.

446 (I) qPCR for atrial (NR2F2) and ventricle MYL7) marker genes show the iPSC-CM are
447 ventricle-type.

448 (J) *MYH6/MYH7* transcript ratio is increased in Group II iPSC-CM, indicating cardiomyocyte
449 maturation defect. Note this ratio is reversed in mice vs. human, as the major ventricular myosin
450 heavy chain in mice is *Myh6*, and *MYH7* in human.

451 (K) Ki67 immunostaining showed decreased proliferation in Group II iPSC-CM.

452 (L, M) Quantification of myofibril organization showed myofibrillar disarray (L) in cTnT (Green)
453 and α -actinin (Red) positive human iPSC-CM (M).

454 (N-P) Beat frequency (N), and visualization (O) and quantification of calcium transients (P) in
455 iPSC-CM showed functional deficits in Group II iPSC-CM.

456 (Q-S) Quantification of contractile function in individual iPSC-CM showed decreased fractional
457 shortening (Q), contraction rate (R) and relaxation rate (S) in Group II iPSC-CM.

458 Data shown are mean \pm SEM using Student's t-test or ANOVA. For box plots, median/min/max are
459 shown with Kruskal-Wallis statistics. Number of Control, Group I, Group II subjects analyzed (H-

460 S): (I) n=3,3,3 subjects. (J) n=3,5,3 subjects. (K, L,N) n=3,6, 3 subjects. (P) n=3,6,4 subjects. (Q-
461 S) n=3,4,4 with n=17,23,38 cardiomyocytes respectively.

462

463 **Figure 2. Mitochondrial dynamics and respiration defects in HLHS iPSC-CM.**

464 (A) Measurement of $\Delta\Psi_m$ in human iPSC-CM using TMRE and MTG staining.

465 (B) Seahorse Analyzer OCR measurement showed mitochondrial respiration defects in the HLHS
466 iPSC-CM.

467 (C) MitoSOX staining show elevated mitochondrial reactive oxygen species (ROS) in Group II
468 HLHS iPSC-CM

469 (D,E) TUNEL labeling and γ -H2AX staining show increased apoptosis (D) and DNA damage (E)
470 in Group II iPSC-CM.

471 (F,G) Mitotracker red staining showed increased linkage constant (see Methods), indicating
472 hyperfused mitochondria in Group II iPSC-CM

473 (H) qPCR of key genes regulating mitophagy and mitochondrial dynamics.

474 (I) LysoTracker Deep Red-staining of lysosomes showed lysosome reduction in Group II iPSC-
475 CM.

476 (J) Basal OCR (>3 duplicates) of explanted heart tissue from two 19-year-old HLHS patients and
477 a 15 year old cardiomyopathy patient with doxorubicin cardiotoxicity were assessed using the
478 Seahorse Analyzer

479 (K). Respiratory control ratio (RCR) was obtained for 2 Control and 2 HLHS neonatal patient
480 using cell extracts from explanted heart tissue. V_{max} was measured using succinate as a substrate
481 and two concentrations of ADP.

482 Bar graphs show mean \pm SEM with ANOVA. Number of Control, Group I, Group II subjects
483 analyzed respectively in (A-I): (A, D) n=3,6,3 subjects. (B, C,F) n=3,5,3 subjects,(E) n=3,4,3
484 subjects. (H) n=3,3,3 subjects (I) n=3, 4, 3 subjects.

485 **Figure 3. HLHS iPSC-CM with failed antioxidant response show cytoplasmic localization of**
486 **NRF2, YAP1, and PITX2**

487 (A) qPCR showed key antioxidant genes and HIF pathway are up regulated in Group I iPSC-CM,
488 and either unchanged or downregulated in Group II iPSC-CM.

489 (B-E) Immunostaining show defect in NRF2, PITX2, YAP and β -catenin nuclear localization in
490 Group II iPSC-CM (see FigS6 G). N/C = nuclear to cytoplasmic ratio.

491 (F) qPCR quantification of YAP and YAP/ β -actinin downstream target genes.

492 (G) Diagram summarizing HLHS associated defects in mitochondrial dynamics with elevated ROS
493 and failed antioxidant response with failure in NRF2, YAP, and YAP/PITX2 nuclear translocation.

494 (A, F) show mean \pm SEM with one-way ANOVA. Box plot with median/min/max shown with
495 Kruskal-Wallis statistics. n=3 control, 3 Group I, 3 Group II subjects.

496 Number of Control, Group I, and Group II subjects analyzed: (B, C) n=130, 117, 64 CM. (D) n=90,
497 78, 79 CM. (E) n=44, 15, 17 CM

498 **Figure 4. Inhibition of mitochondrial membrane permeability rescues mitochondrial**
499 **respiration and apoptosis.**

500 (A-H) Sildenafil (Sil) rescued Group II iPSC-CM including $\Delta\Psi_m$ (A), maximum OCR (B),
501 mitochondrial ROS (C), NO level (D), cell proliferation (E), apoptosis (F), and YAP (G) and β -
502 catenine (H) nuclear localization.

503 (I-L) Treatment with bongkreikic acid (BKA), but not carboxyatractyloside (CAT) rescued $\Delta\Psi_m$
504 (I), maximum OCR (J), mitochondrial ROS (K) and YAP nuclear localization (L).

505 Bar graphs show mean \pm SEM, analyzed by one-way ANOVA, and box plot with median/min/max
506 analyzed by Kruskal-Wallis. $n\geq 3$ independent repeats. Subjects analyzed: Control $n=3$, Group I
507 $n=4$ or 5, and Group II, $n=3$ or 4.

508 **Figure 5. Single cell RNAseq showed mitochondrial pathways associated with early-HF.**

509 (A) Single cell RNAseq data yielded 9 distinct clusters (See Figure S5E). Clusters 0,1, and 5
510 are comprised of well differentiated cardiomyocytes of increasing maturation. Clusters 4 and 6
511 correspond to proliferating cardiomyocytes at G2/M and S phase (also see Figure S5E). Cluster 2
512 include cardiomyocytes undergoing apoptosis, while Cluster 7 exhibit evidence of ER stress with
513 UPR (Figure S5E). In Clusters 3 and 8, enrichment for oxidative phosphorylation and genes related
514 to hypertrophic cardiomyopathy are observed (see Spreadsheet 2).

515 (B) DEGs recovered in each cluster with pairwise comparisons.

516 (C-E) Pathway enrichment of with DEGs in pairwise patient group comparisons in Clusters 0, 1
517 and 5.

518 (F). Heat map of DEGs from all pairwise comparisons for Clusters 0,1, and 5 and the top Biological
519 Processes recovered.

520 (G). Percentage of DEGs that are mitochondrial related is shown for each group in F. The n
521 represents number of mitochondrial DEGs observed.

522 (H). Heat map of mitochondrial related DEGs in clusters 0, 1 and 5 and the top Biological
523 Processes recovered.

524 (F, H) Color scale showed relative maximum and minimum value. Grayscale showed the adjust p
525 value (-log₁₀FDR) of each GO term and circle size showed the count of genes in each GO term.

526 (I) Hierarchical clustering based on DEGs from Group II (7052 and 7042) vs. Group I (7464).

527 Asterisk (*) denotes region with 28 DEGs upregulated only in 7052 (Spreadsheet 2).

528 (J) Violin plot showing transcript expression for 6 of the 28 DEGs from panel I.

529 **Figure 6. ER stress in the iPSC-CM and its suppression rescued mPTP closure and apoptosis.**

530 (A) ER stress was recovered as top pathway in Cluster 7.

531 (B) Real time PCR confirmed elevated expression of ER stress marker genes in Group II

532 (7042,7052) iPSC-CM.

533 (C-H) Treatment with molecular chaperone TUDCA, an ER stress inhibitor, rescued $\Delta\Psi_m$ (C),

534 ROS (D), NO level (E). YAP nuclear localization (F), and restored cell proliferation (G) and

535 suppressed apoptosis (H)

536 Bar graphs show mean \pm SEM with Student's t-test. Box plots show median and minimum-

537 maximum, with Mann-Whitney statistical test. (B) n=3 independent repeats for each sample. (C-

538 H) n \geq 3 independent repeats for each bar. Subjects analyzed: Control n=3, Group I n=4 or 5, and

539 Group II, n=2 (7042 and 7052).

540 **Figure 7. Damaging variants in mitochondrial and Hippo related pathways**

541 (A,B) Protein-protein interactome constructed with four genes (*OXAIL*, *NNMT*, *NEU3*, *ALDH7A*;
542 blue triangle nodes) to explore interconnections with the Hippo pathway recovered many genes
543 related to Hippo and Wnt signaling and also mitochondrial and cardiac related genes
544 (C) Pathway enrichment rendered using Metascape comprising genes recovered with extreme
545 unique variants from 41 HLHS patients. Size of the collective node slice represents percentage of
546 genes originating from the corresponding gene list.
547 (D) Pathway enrichment related to the 19 mitochondrial genes recovered from the unfavorable
548 outcome HLHS patients that intersected with the MitoCarta inventory of mitochondrial genes (see
549 overlapping genes in Supplementary Spreadsheet 3).
550 (E) Mitochondrial transcript expression in cardiomyocytes from human heart tissue at 5-15 weeks
551 gestation from scRNAseq data of Cui, et al (Cui *et al.*, 2019). Size of the circle corresponds to
552 percentage of cells expressing the gene (Exp%) and the color show average expression values with
553 Z-transform.

554 **ACKNOWLEDGMENTS**

555 This work was supported by funding from University of Pittsburgh (C.W.L), NIH HL132024
556 (CWL), HL142788 (CWL, MT), NIH HL144776 (GP), DOD PR140183 (CWL), postdoctoral
557 fellowship (X.X.) jointly funded by the American Heart Association and
558 the Children's Heart Foundation. Some human heart tissues were obtained from the Molecular
559 Atlas of Lung Development Program (LungMAP) Consortium distributed by Human Tissue Core
560 (HTC) supported by NIH grants HL122700 and HL148861 (G. H. Deutsch, T. J. Mariani, and G.
561 S. Pryhuber). Donor tissue was supplied through the United Network for Organ Sharing. We thank
562 the staff of the HTC including Heidie Huyck and Cory Poole. We are grateful to families who
563 generously give such precious gifts to support this research.

564 **AUTHOR CONTRIBUTIONS**

565 Study design: C.W.L. and X.X; miPSC and hiPSC reprogramming: iPSC-CM differentiation,
566 cardiomyocyte proliferation and apoptosis, cardiomyocyte and mitochondrial function
567 measurements, drug screening and data analysis: X.X; Single cell RNAseq and data analysis:
568 X.X,K.J,B.A,H.Y.,C.W.L.,A.S.B,D.K; human patient clinical data analysis: J.I.L,P.A; recruitment
569 of subjects and human tissue sample collection: C.W.L.,J.I.L.,P.A.,G.B, G.A.P; human heart tissue
570 analysis: G.B,G.A.P.,X.X.; Seahorse measurement support: S.S.S; mouse fetal ultrasound imaging
571 and mouse phenotyping: X.L.,X.X.; mitochondrial staining support and analysis:
572 X.X.,T.N.F.G.A.P; iPSC-CM sarcomere video analysis: P.N, J.C, C.K.K; human exome
573 sequencing analysis: W.Z; protein network analysis, K.B.K, M.K.G.; statistics: X.X; manuscript
574 preparation: C.W.L, X.X, A.S.B, K.J, B.A, G.A.P., J.I.L, R.A.D, M.T., M.K.G., W.Z and T.N.F.

575

576 **COMPETING INTERESTS STATEMENT**

577 The authors declare no competing financial interests.

578

579 **EXPERIMENTAL MODEL AND SUBJECT DETAILS**

580 **Mouse Strain**

581 E13.5-E14.5 Ohia HLHS mouse (*Sap130m/m;Pcdha9m/m*) or CRISPR HLHS mouse
582 (*Sap130m/m;Pcdha9m/m*) and littermate controls were used for primary cardiomyocytes explants
583 from heart tissue. Mouse embryo fibroblasts used for mouse iPSC generation were generated from
584 E14.5 – 17.5 mouse embryos (**See Supplemental Spreadsheet1**). All mice were housed, treated,
585 and handled in accordance with the guidelines set forth by the University of Pittsburgh Institutional
586 Animal Care and Use Committee and the National Institutes of Health’s Guide for the Care and
587 Use of Laboratory Animals.

588 **Human Blood, Cells, and Surgical Tissue**

589 Cells, heart tissue and blood were obtained from HLHS patients recruited from Children’s
590 Hospital of Pittsburgh of UPMC with informed consent under a human study protocol approved
591 by the University of Pittsburgh Institutional Review Board (Supplemental Spreadsheet 1). For
592 infants and minors, informed consent was obtained from the legal guardian. Some human heart
593 tissues were obtained from the Molecular Atlas of Lung Development Program (LungMAP)
594 Consortium distributed by Human Tissue Core (HTC). Donor tissue was supplied through the
595 United Network for Organ Sharing for Western blot and isolated mitochondrial OCR
596 measurements.

597 **METHOD DETAILS**

598 **Production of patient iPSC cells**

599 Mouse embryonic fibroblasts were reprogrammed using the CytoTune-iPS Sendai
600 Reprogramming kit(Fusaki et al., 2009). Human fibroblasts or lymphoblastoid cells were
601 transfected with four episomal plasmids(Okita et al., 2011) using electroporation. iPSCs clones

602 were identified by immunofluorescent staining of pluripotency marker Oct4 and Nanog and qPCR
603 analysis of stem cell markers (**Supplemental Figure S2B**)(Xu et al., 2013). All antibody and
604 primer sequence information are provided in **Supplemental Spreadsheet 1**

605 Several independent iPSC clones were isolated for four of the HLHS patients, and analysis
606 conducted with these independent clones generally yielded similar results (see **Figure S2D**). While
607 independent iPSC clones from one subject are often used to demonstrate reproducibility of
608 findings, one study using transcriptome profiling showed the importance of using iPSCs of
609 different parental origin rather than multiple sister iPSC clones to distinguish disease-associated
610 mechanisms from genetic background effects in disease modeling(Schuster et al., 2015).

611 **Production of iPS derived cardiomyocytes**

612 The iPSC cells were seeded on BD Matrigel pre-coated plates for 2-3 days under mTESR1
613 media then switched to CDM3 media consisting of RPMI 1640, BSA, 213 µg/ml Vitamin C
614 (Ascorbic acid) and 6 µM CHIR99021(Burridge et al., 2014). After 2 days the media was replaced
615 with CDM3 Media containing RPMI 1640, BSA, 10 µM XAV939, 213 µg/lm Vitamin C, and
616 BSA. Finally, ~14 days after initiating reprogramming, beating cells are observed and further
617 analyzed in the following days (Day18-22).

618 **Immunofluorescence Staining**

619 Cells were fixed with 4% paraformaldehyde with 0.1% Triton X-10, followed by blocking in
620 5% goat serum, then staining overnight with primary antibody in 0.5% bovine serum
621 albumin/phosphate-buffered saline (BSA/PBS). After washing in PBS, incubation with secondary
622 antibody was performed in 0.5% BSA/PBS for 1 hour at room temperature and nuclei were stained
623 with 2 µg/ml Hoechst 33342 (Life Technologies). Images were acquired using the Leica SP8
624 confocal or Leica DMI6000-SD microscopes. Antibody information in **Supplemental**

625 **Spreadsheet 1**

626 **Analysis of mitochondrial calcium transients**

627 iPSC-CMs cultured in chamber slides were loaded with 1 μ M Rhod-2 (Molecular Probes, Life
628 Technologies, Carlsbad, CA, USA) in Hank's balanced salts modified buffer (HBSS, pH 7.4) for
629 15 minutes at 37°C and washed twice for 15 minutes in HBSS. The slides were placed on a
630 temperature-regulated microscope stage and kept at 37°C. Fluorescence images were acquired
631 using the ImageJ time series analyzer package (NIH, Bethesda, MD; Version: 2.0.0-rc-69/1.52K)
632 together with Leica DMI6000-SD fluorescence microscope. The data shown represent the average
633 of Rhod-2 intensity for 3 controls and 10 HLHS patients iPSC-CMs from three independent
634 experiments.

635 **Analysis of sarcomere contractility in iPSC-CM**

636 Single iPSC-CM cell videos were collected by Leica DMI 3000B microscope and videos of
637 human iPSC-CM (200 Hz) containing striated sarcomere were analyzed using a custom MATLAB
638 code (available upon request) written to apply the fast Fourier transform (FFT) algorithm to each
639 frame (approximately 1400 frames per video) to compute the spatial frequencies of the sarcomeres.
640 The frequency (f_0) of the highest amplitude peak of the FFT within a user defined range was
641 identified, and sarcomere length (L) in each frame was calculated by taking the reciprocal of f_0 ,
642 $L = \frac{1}{f_0}$. The user defined range was determined and optimized to ensure that the maximum and
643 minimum measured sarcomere lengths always occurred within this range. The sarcomere length
644 in units of pixels was then converted to units of micrometers, $1\mu\text{m} = 4.58$ pixels (100X
645 magnification video), and plotted as a function of time (seconds). From the plots of sarcomere
646 length versus time, the point of maximum sarcomere length immediately before contraction (t_1 ,
647 max), minimum sarcomere length (Systolic length) during contraction (t_2 , min), and maximum

648 sarcomere length (Diastolic length) immediately after contraction (t_3 , max) were identified for each
649 contraction. Fractional shortening (FS) was calculated as $FS = \frac{max-min}{max}$, contraction rate (CR)
650 was calculated as $CR = \frac{max-min}{t_2-t_1}$, and relaxation rate (RR) was calculated as $RR = \frac{max-min}{t_3-t_2}$.

651 **RNA extraction, real-time PCR, and transcript splicing analysis**

652 Total RNA was isolated using the miRNeasy micro-Kit (QIAGEN) with on-column DNase I
653 digestion (QIAGEN). cDNA was prepared with high-capacity RNA to cDNA kit (Applied
654 Biosystems). Real-time PCR was conducted using 7900HT Fast Real Time PCR System. All
655 primer sequence information is provided in **Supplemental Spreadsheet 1**

656 **Seahorse Analyzer analysis of oxygen consumption rate**

657 For cell oxygen consumption rate (OCR) quantification, 20,000 iPS-CMs or 20000 iPSCs were
658 seeded into each well of a Seahorse XFe96 cell culture plate and cultured for 2 days for adherence
659 to the culture plate. On day of measurement, the medium was changed to pre-warmed Seahorse
660 assay medium, and OCR determined using the Seahorse XF Cell Mito Stress Kit (Agilent). Basal
661 respiration was measured in unstimulated cells. Afterwards, oligomycin (1 μ M) was added to
662 quantify respiration coupled to ATP production and proton leak followed by carbonyl cyanide-4-
663 (trifluoromethoxy)-phenylhydrazone (FCCP; 1 μ M) injection to assess maximal cellular
664 respiration (respiratory capacity). Finally, antimycin A (1 μ M) and rotenone (1 μ M) were used to
665 assess non-mitochondrial respiration. For mouse and human heart tissue OCR quantification, 2mm
666 X 2mm heart tissue pieces were seeded into each well of a Seahorse XF24 islet capture microplate
667 and OCR were measured using the same Seahorse XF Cell Mito Stress Kit to obtain the basal
668 respiration rate in unstimulated cells during two cycles of measurement.

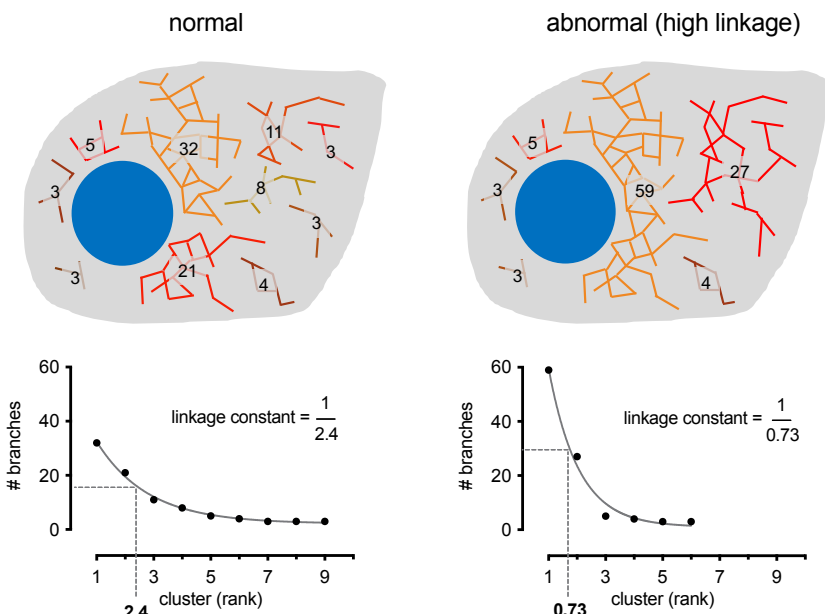
669 **Analysis of inner mitochondrial transmembrane potential**

670 Embryonic left and right ventricles were dissociated with papain to generate primary
671 cardiomyocytes for live imaging as previously described (Hom *et al.*, 2011). Briefly, this entailed
672 loading live explanted cardiomyocytes, iPSC, and iPSC-CM for 35 minutes with
673 tetramethylrhodamine ethyl ester (TMRE, 20 nM, Invitrogen, Cat# T-669) and Mito Tracker Green
674 (MTG, 200 nM, Invitrogen, Cat# M-7514) in Hepes-Tyrode's buffer, washed, and equilibrated for
675 20 minutes in the same buffer. The live cells were then imaged using epifluorescence microscopy.
676 Mitochondrial membrane potential ($\Delta\psi_m$) was quantified as the ratio of TMRE to MTG intensity
677 (Galmiche *et al.*, 2011).

678 **Mitochondrial network analysis**

679 MitoTracker Red (100 μ M) was loaded into live cells following manufacturer's
680 recommendations, and then cells were fixed in 4% paraformaldehyde/PBS at 37°C for 15 minutes.
681 Cells were permeabilized in 0.2% Triton X-100/PBS for 10 minutes and then immunostained for
682 cTnT while DNA was labeled with Hoechst. Mitochondria were imaged using a Leica SP8
683 confocal with a 40x / 1.3NA objective. Acquisition settings and deconvolution were done with the
684 guidance of SVI Huygens software, and images were post-processed in ImageJ (NIH, Bethesda,
685 MD; Version: 2.0.0-rc-69/1.52K) with unsharp mask (radius 2; mask weight 0.7), background
686 subtraction, and the tubeness filter (sigma = 0.25 microns) to highlight mitochondrial filaments.
687 Mitochondria were segmented with Skeletonize 2D/3D. Mitochondrial networks were then
688 analyzed ("Analyze Skeleton") using BoneJ. Clusters with 20 branches or more were used for
689 measuring average branch length and linkage statistics. To quantify the degree of mitochondrial
690 consolidation, clusters were ranked from most to least branches (see graphs) and a mono-
691 exponential decay curve is fit to the resulting data. The curve's decay constant is then inverted so
692 that higher values reflect more-linked mitochondrial networks.

693



694

695 Mitochondrial DNA copy number assays

696 DNA was extracted from human iPSC-CM. qPCR was performed and mitochondrial DNA
697 copy number was determined by normalizing results from primers targeted to mtDNA-tRNA-Leu
698 (Forward: 5'- CAC CCA AGA ACA GGG TTT GT-3' and Reverse: 5'- TGGCCATGG GTA TGT
699 TGT TA -3') against results from primers targeted to nuclear B2-microglobulin (Forward: 5'- TGC
700 TGT CTC CAT GTT TGA TGT ATC T-3' and Reverse: TCT CTG CTC CCC ACC TCT AAG
701 T-3'(Rooney et al., 2015).

702 Reactive oxygen species, nitric oxide and lysosome measurements

703 To quantify reactive oxygen species (ROS), nitric oxide level and lysosome abundance, iPSC-
704 CMs were incubated at 37 °C for 30 minutes with 5 μ M MitoSOX, 5 μ M DAF-FM diacetate and
705 1 μ M LysoTracker Red DND-99 (Life Technologies), respectively. For NO measurement,
706 additional 15–30 minutes incubation could complete de-esterification of the intracellular diacetates.
707 CD172a(SIRP α/β) was used as a human iPSC-CM marker (Dubois et al., 2011). Live cell

708 fluorescent imaging was conducted using the Leica DMI6000-SD microscope.

709 **Human heart tissue and iPSC-CM Western blotting**

710 LV and RV tissue or iPSC-CM were homogenized and processed for Western blotting using a
711 ChemiDoc (Biorad) with Image J image processing (Beutner et al., 2017; Beutner et al., 2014).
712 Antibodies from Abcam and BioRad were used and included: OXPHOS Rodent Cocktail
713 (ab110413), AC (#154856), Starbright 700 (anti-mouse), Starbright 520 (anti-rabbit).

714 **Isolation of mitochondria and oxygen consumption assay**

715 Mitochondria were isolated on ice from fresh or frozen tissue (~140 mg) in isolation medium by
716 homogenization and differential centrifugation and resuspended in EGTA/EDTA-free isolation
717 (Beutner *et al.*, 2017; Beutner *et al.*, 2014). Oxygen consumption was measured at room
718 temperature in respiration medium with a Clark oxygen electrode (Hansatech) using published
719 protocols. Cytochrome c (50 μ M) and atractyloside (100 μ M) were used to test mitochondrial
720 membrane integrity. Substrate-mediated respiration (state 2 or V₀), maximal respiration (state 3
721 or V_{max}), and RCR (V_{max} over V₀) were calculated.

722 **Single-cell RNA sequencing**

723 Previous study proved there is no significance difference between iPSC-CM from day 21 and
724 day 30 (funakoshi et al., 2018), hence, the iPSC-CM differentiated at day 22 were chosen as
725 scRNAseq samples. The iPSC-CM from three patients and one control was prepared for single cell
726 RNAseq. The iPSC-CMs were disaggregated using cold active protease [10 mg/ml Bacillus
727 Licheniformis protease; Creative Enzymes NATE0633] and 125 U/ml DNase (Applichem, A3778)
728 incubated on ice with trituration 5-7 minutes, then 5% bovine serum albumin (BSA) was added,
729 and cells were filtered by 100 μ m cell strainer and the cells pelleted, then re-suspended in 200 μ l
730 PBS/BSA. Trypan blue exclusion was used to quantify cell viability, and the volume was adjusted

731 to 200,000 cells/ml for 10X chromium single-cell RNA-seq. Pair-end library preparation was
732 carried out using the V3 version (10X Genomics). Single-cell droplet libraries from ~10K cells
733 from each suspension were generated using the 10X Genomics Chromium controller with the
734 Chromium Single Cell 3' GEM Library and Gel Bead Kit v.3 and the Chromium Chip B Single
735 Cell kit (1 GEMs per sample, expected recovery ~6k cells per GEM). All samples were barcoded
736 with the Chromium i7 Multiplex Kit. All libraries were pooled and sequenced across two lanes of
737 a HiSeq4000, 150bp paired end reads with a target coverage of 20k fragments per cell. All samples
738 were uniquely indexed, mixed, and evenly distributed into the Illumina HiSeq 4000 for sequencing.

739 **Single-cell RNA-Sequencing Data Analysis**

740 Single-cell sequencing data was processed using the Cell Ranger (version 3.1.0) count pipeline
741 using the human reference genome GRCh38 and annotations from Ensembl (version 93). Quality
742 control and filtering were performed using scater (McCarthy et al., 2017) (v1.18.6). For each
743 sample, cells with library size less than 500, number of detected genes less than 300 or greater than
744 6,000, or mitochondrial percentage greater than 4 times the median absolute deviation (MAD)
745 from the median value were excluded. Additionally, top 3% cells ranked by the doublet score
746 (hybrid) calculated using the scds R package (Bais and Kostka, 2020) (v1.6.9) were excluded.
747 Only non-ribosomal genes with at least 1 count in ≥ 5 cells were considered. We adapted the
748 approach of Kannan et al. [<https://doi.org/10.1101/2020.04.02.022632>] for cell type classification
749 using SingleCellNet(Tan and Cahan, 2019) (v0.1.0) and further limited to cells classified as
750 "cardiac muscle cells" yielding a data for 13,954 genes across 8,094 cells. We performed
751 downstream analyses using the Seurat package (Stuart *et al.*, 2019). To focus on high-quality CMs,
752 we further removed cells with total library size less than 1,400 or number of detected genes ≤ 800 ,

753 or percentage of mitochondrial gene counts greater than 20%. This yielded a final set of 877, 1,718,
754 1,434, 374 cells for 1053, 7042, 7052 and 7464, respectively, for downstream analysis.

755 We normalized total count per cell to 10,000 and find top 2000 highly variable genes in each
756 sample. Integration of cells from different samples and batch correction were performed using
757 IntegrateData function in Standard procedure of Seurat 3. Scaled data after integration was used
758 for principal component analysis (PCA) and top 30 dimensions were used for neighbor detection
759 and Louvain clustering (resolution = 0.5). UMAP was drawn for the visualization of single-cell
760 data in reduced dimensions.

761 Differentially expression analysis was conducted using student t-test in Scanpy(Wolf et al.,
762 2018). We compared differentially expressed genes of clusters and sample groups, as well as
763 samples and sample groups per cluster (Figure 5C-F,G, S5F). Genes with $FDR < 0.05$ in tests were
764 selected as DEGs. ToppGene(Chen et al., 2009) was used for gene enrichment analysis and Gene
765 Ontology (Biological Process) terms and coexpression of MSigDB were used for annotations of
766 gene lists. The strength of associations was represented by $-\log_{10}(FDR_{ToppGene})$ (Figure 5C-
767 F,G). Gene modules of cardiomyocyte clusters were generated using 200 most significantly
768 upregulated genes (Figure S5E) and their top enriched Gene Ontology (Biological Process) terms
769 were used for annotating cluster identities. Similarity between these clusters were evaluated using
770 Pearson correlation of genes in gene modules. Cell cycle scores were calculated in Seurat using
771 CellCycleScoring function and cell cycle phases were inferred accordingly (Figure S5C).

772 **Whole exome sequencing analysis**

773 Whole-exome capture was carried out on 6 Caucasian HLHS subjects with iPSC and 41 HLHS
774 subjects (including the 6 HLHS subjects) at BGI Americas. Genomic DNA from venous blood
775 was captured with Agilent V4 Exome Capture kit. Sequencing was performed on the Illumina

776 HiSeq2000 platform with 100 paired-end reads, or the Illumina HiSeq4000 with 150 paired-end
777 reads at 100× coverage. Sequence reads were mapped to the reference genome (hg19) with BWA-
778 MEM(Arakawa et al., 2010) and further processed using the GATK(McKenna et al., 2010) Best
779 Practices workflows, which include duplication marking, and base quality recalibration. Single
780 nucleotide variants (SNVs) and small indels (InDels) were detected using GATK haplotypeCaller
781 and annotated by Annovar(Wang et al., 2010). High quality variants were recovered that: 1)
782 passed GATK Variant Score Quality Recalibration (VSQR); 2) have minimum 5 supported reads;
783 3) have genotype quality ≥ 20 or 60 for SNVs or InDels, respectively; 4) SNVs or InDels not
784 within 10bp or 5bp of an indel, respectively.

785 Variants with minor allele frequency (MAF) was less than 0.01 in GnomAD exome
786 (Karczewski et al., 2020)or Kaviar database were retained for downstream analyses. Only loss-of-
787 function (LoF) mutations (nonsense, canonical splice-site, frameshift indels, and start loss), likely
788 damaging missense variants (D-Mis) and non-frameshift indels were considered potentially
789 damaging. Missense variants were considered likely damaging if it was predicted to be damaging
790 by at least three out of nine prediction scores available via dbNSFP v3.5a (Liu et al., 2016). All
791 filter processes are shown in **Figure S7**.

792 **Functional enrichment and interactomes analysis**

793 Webgestalt KEGG pathway analysis (<http://webgestalt.org/>) was performed for unique LoF
794 variants from 6 HLHS cohort. The interactomes of the four genes harboring unique variants in the
795 HLHS unfavorable patient was assembled by including their protein-protein interactions (PPIs)
796 collected from BioGRID (Stark et al., 2011) and HPRD (Prasad et al., 2009), and novel PPIs
797 predicted by High-precision PPI Prediction (HiPPIP) model (Ganapathiraju et al., 2016) focusing
798 on short path connections to the Hippo pathway. Hippo pathway genes were extracted from KEGG

799 (Kanehisa et al., 2008). Enrichment Analysis Tool available on Gene Ontology (GO) website
800 which uses PANTHER (Ahmad et al., 2013) on the backend, was used to find biological process
801 terms associated with the interactome genes with statistical significance. It computes fold
802 enrichment of the genes in the input list over the expected value. Fold enrichment >1 and fold
803 enrichment <1 showed that the annotation is overrepresented and underrepresented in the list
804 respectively. It presents p-value determined by Fisher's exact test with FDR correction, and a cut-
805 off of 0.05 was used to select significantly enriched annotations.

806 **QUANTIFICATION AND STATISTICAL ANALYSIS**

807 Standard statistical analyses were performed using GraphPad Prism 9. D'Agostino & Pearson
808 normality test and Shapiro-Wilk normality test were used to test if the data had a Gaussian
809 distribution. For Gaussian distribution, data are presented as bar graphs and expressed as
810 mean \pm SEM, either Unpaired t-test (Two-tailed) or One-way ANOVA (FDR B&Y correction were
811 used for multiple comparisons) were applied. Data without Gaussian distribution showed by box
812 plot (Line at median and minimum-maximum were represented by the top /bottom of box), either
813 non-parametric Mann-Whitney test (Two-tailed) or Kruskal-Wallis tests (FDR B&Y correction
814 were used for multiple comparisons) were used. The experiments were not randomized. The inves-
815 tigators were not blinded to allocation during experiments and outcome assessment.

816

817 **SUPPLEMENTAL INFORMATION**

818 **Supplemental Figure 1: Mitochondrial defects in the HLHS mouse heart tissue and HLHS**
819 **mouse iPSC-CM.** Related to Figure 1.

820 **Supplemental Figure 2: Generating iPSC and iPSC-CM from HLHS patients and control**
821 **subjects** Related to Figure 1.

822 **Supplemental Figure 3: Mitochondrial defects and altered Hippo signaling** Related to Figure
823 2&3.

824 **Supplemental Figure 4: Inhibition of the mitochondrial permeability transition pore rescues**
825 **mitochondrial respiration and YAP1 nuclear localization.** Related to Figure 4.

826 **Supplemental Figure 5: Analysis of HLHS patient iPSC-CM using single-cell RNAseq**
827 Related to Figure 5.

828 **Supplemental Figure 6: Protein-Protein Interactome of Genes Highly Expressed Only in**
829 **Patient 7052.** Related to Figure 5.

830 **Supplemental Figure 7: Whole exome sequencing analysis of pathogenic variants show**
831 **enrichment for metabolic-mitochondrial pathways in Group II HLHS patients** Related to
832 Figure 7.

833

834

835

836

837

838

839

840 **Supplemental Spreadsheet 1: Patient information, iPSC production, antibodies, and primer**
841 **sequences. Related to STAR Methods.**

842 1. miPSCs generated and used in this study

843 2. HLHS patient medical history

844 3. Patient iPSCs reprogramming

845 4. Human and mouse primer sequences.

846 **Supplemental Spreadsheet 2: Single cell RNAseq related information. Related to Figure5,6.**

847 1. Marker gene list for C0-8 (Figure S5 E)

848 2.1-2.9. GO enrichment analysis for Cluster 0-8 (Figure S5 E)

849 2.10. HCM related genes in Clusters C3 and C8 (Figure 5 A)

850 3.1. DEG No. in Each Cluster (Figure 5 B)

851 3.2-3.10. GO enrichment analysis of DEG in C0/C1/C5 under different comparisons (Figure 5 C-
852 E)

853 4.1 All DEGs in Figure 5F

854 4.2 Toppgene of Control 1053 DEGs (Figure 5F)

855 4.3 Toppgene of Patient 7464 DEG (Figure 5F)

856 4.4 Toppgene of Group II 7042/7052 Shared DEG (Figure 5F)

857 4.5 Toppgene of Patient 7042 DEG (Figure 5F)

858 4.6 Toppgene of Patient 7052 DEG (Figure 5F)

859 5.1. Mitochondrial DEGs (Figure 5H)

860 5.2 Toppgene of Control 1053 Mitochondrial DEGs (Figure 5H)

861 5.3. Toppgene analysis of Patient 7464 Mitochondrial – DEGs (Figure 5H)

862 5.4. Toppgene of Group II Mitochondrial-DEG (Figure 5H)

- 863 5.5. Toppgene of Patient 7042 Mitochondrial-DEG (Figure 5H)
- 864 5.6. Toppgene of Patient 7052 Mitochondrial-DEG (Figure 5H)
- 865 6. Patient 7052 - 28 upregulated DEGs (Figure 5G)
- 866 7.1. Protein-Protein Interactome network genes (Figure S6A)
- 867 7.2. PPI BiNGO Biological Process Pathway Enrichment (Figure 5I)
- 868 8.1-8.2. GO enrichment analysis of DEG of Group II VS Control in C7 (Figure 6A)
- 869 **Supplemental Spreadsheet 3: Whole exome sequencing and interactome analysis related**
- 870 **information. Related to Figure7.**
- 871 1. Description
- 872 2. Unique LoF genes from Group II patient (Figure 7A)
- 873 3. LoF (loss of function) variants from Group II patient (Figure 7A)
- 874 4. Webgestalt/KEGG pathway enrichment of unique LoF genes from Group II patient (*OXAIL*,
- 875 *NNMT*, *NEU3*, *ALDH7A1*) (Figure 7A)
- 876 5. Protein-protein interactome GO Biological Processes
- 877 6. GO Biological Processes in Figure 7B
- 878 7. Genes in GO Biological Processes in Figure 7B.
- 879 8. Unique gene with variants in 41 HLHS cohort (Figure 7C)
- 880 9. Extreme variant list in 41 HLHS cohort (Figure 7C)
- 881 10. Metascape-GoEnriched (Figure 7C)
- 882 11. Mitochondrial gene list (Figure 7D)
- 883 12. Damaging variants in mitochondrial-related genes (Figure 7D)
- 884 13. Overlapping mitochondrial and unique genes in 41 HLHS cohort (Figure 7D)
- 885 14. Toppgene analysis of those 19 overlapping genes (Figure 7D)

886 **SUPPLEMENTAL VIDEO LEGEND**

887 **Supplemental Videos**

888 Sup-video-1_hips-cm_beating-Related to Figure1

889 Sup-video-2_hips-cm_Ca-Related to Figure1

890 Sup-video-3_hips-cm_single_cell-Related to Figure1

891

892 **Sup-video-1_hips-cm_beating:** Videomicroscopy showing contraction of human iPSC-CM. The

893 iPSC-CM from control subject and Group I beat faster than iPSC-CM from Group II. Scale bar =

894 250 μm .

895

896 **Sup-video-2_hips-cm_Ca:** Calcium transients in the iPSC-CM are visualized using Rhod-2. Note

897 faster propagation of calcium transients in iPSC-CM from control subject and Group I patients as

898 compared to that of Group II. Scale bar = 250 μm .

899

900 **Sup-video-3_hips-cm_single_cell:** Videomicroscopy recording of individual beating iPSC-CM

901 from control subject, Group I and Group II patients. Robust contractions are seen in

902 cardiomyocytes from control and Group I, but only weak contractions are seen in Group II. Scale

903 bar = 10 μm .

904

905 REFERENCE

- 906 Ahmad, A., Maitah, M.Y., Ginnebaugh, K.R., Li, Y., Bao, B., Gadgeel, S.M., and Sarkar, F.H.
907 (2013). Inhibition of Hedgehog signaling sensitizes NSCLC cells to standard therapies through
908 modulation of EMT-regulating miRNAs. *J Hematol Oncol* 6, 77. 10.1186/1756-8722-6-77.
- 909 Alsoufi, B., Mahle, W.T., Manlihot, C., Deshpande, S., Kogon, B., McCrindle, B.W., and Kanter,
910 K. (2016). Outcomes of heart transplantation in children with hypoplastic left heart syndrome
911 previously palliated with the Norwood procedure. *J Thorac Cardiovasc Surg* 151, 167-174, 175
912 e161-162. 10.1016/j.jtcvs.2015.09.081.
- 913 Arakawa, K., Kudo, T., Ikawa, M., Morikawa, N., Kawai, Y., Sahashi, K., Lee, J.D., Kuriyama,
914 M., Miyamori, I., Okazawa, H., and Yoneda, M. (2010). Abnormal myocardial energy-production
915 state in mitochondrial cardiomyopathy and acute response to L-arginine infusion. C-11 acetate
916 kinetics revealed by positron emission tomography. *Circ J* 74, 2702-2711.
- 917 Artap, S., Manderfield, L.J., Smith, C.L., Poleshko, A., Aghajanian, H., See, K., Li, L., Jain, R.,
918 and Epstein, J.A. (2018). Endocardial Hippo signaling regulates myocardial growth and
919 cardiogenesis. *Dev Biol* 440, 22-30. 10.1016/j.ydbio.2018.04.026.
- 920 Ascah, A., Khairallah, M., Daussin, F., Bourcier-Lucas, C., Godin, R., Allen, B.G., Petrof, B.J.,
921 Des Rosiers, C., and Burelle, Y. (2011). Stress-induced opening of the permeability transition pore
922 in the dystrophin-deficient heart is attenuated by acute treatment with sildenafil. *Am J Physiol*
923 *Heart Circ Physiol* 300, H144-153. 10.1152/ajpheart.00522.2010.
- 924 Bais, A.S., and Kostka, D. (2020). scds: computational annotation of doublets in single-cell RNA
925 sequencing data. *Bioinformatics* 36, 1150-1158. 10.1093/bioinformatics/btz698.
- 926 Beutner, G., Alanzalon, R.E., and Porter, G.A. (2017). Cyclophilin D regulates the dynamic
927 assembly of mitochondrial ATP synthase into synthasomes. *Sci Rep* 7. ARTN 14488
928 10.1038/s41598-017-14795-x.
- 929 Beutner, G., Eliseev, R.A., and Porter, G.A. (2014). Initiation of Electron Transport Chain Activity
930 in the Embryonic Heart Coincides with the Activation of Mitochondrial Complex 1 and the
931 Formation of Supercomplexes. *PLoS One* 9. ARTN e113330
932 10.1371/journal.pone.0113330.
- 933 Biendarra-Tiegs, S.M., Li, X., Ye, D., Brandt, E.B., Ackerman, M.J., and Nelson, T.J. (2019).
934 Single-Cell RNA-Sequencing and Optical Electrophysiology of Human Induced Pluripotent Stem
935 Cell-Derived Cardiomyocytes Reveal Discordance Between Cardiac Subtype-Associated Gene
936 Expression Patterns and Electrophysiological Phenotypes. *Stem Cells Dev* 28, 659-673.
937 10.1089/scd.2019.0030.
- 938 Burridge, P.W., Matsa, E., Shukla, P., Lin, Z.C., Churko, J.M., Ebert, A.D., Lan, F., Diecke, S.,
939 Huber, B., Mordwinkin, N.M., et al. (2014). Chemically defined generation of human
940 cardiomyocytes. *Nat Methods* 11, 855-860. 10.1038/nmeth.2999.
- 941 Calvo, S.E., Compton, A.G., Hershman, S.G., Lim, S.C., Lieber, D.S., Tucker, E.J., Laskowski, A.,
942 Garone, C., Liu, S., Jaffe, D.B., et al. (2012). Molecular diagnosis of infantile mitochondrial
943 disease with targeted next-generation sequencing. *Sci Transl Med* 4, 118ra110.
944 10.1126/scitranslmed.3003310.
- 945 Chen, J., Bardes, E.E., Aronow, B.J., and Jegga, A.G. (2009). ToppGene Suite for gene list
946 enrichment analysis and candidate gene prioritization. *Nucleic Acids Res* 37, W305-311.
947 10.1093/nar/gkp427.
- 948 Cleves, M.A., Ghaffar, S., Zhao, W., Mosley, B.S., and Hobbs, C.A. (2003). First-year survival of
949 infants born with congenital heart defects in Arkansas (1993-1998): a survival analysis using

950 registry data. *Birth Defects Res A Clin Mol Teratol* 67, 662-668. 10.1002/bdra.10119.

951 Cui, Y., Zheng, Y., Liu, X., Yan, L., Fan, X., Yong, J., Hu, Y., Dong, J., Li, Q., Wu, X., et al. (2019).

952 Single-Cell Transcriptome Analysis Maps the Developmental Track of the Human Heart. *Cell Rep*

953 26, 1934-1950 e1935. 10.1016/j.celrep.2019.01.079.

954 Cyganek, L., Tiburcy, M., Sekeres, K., Gerstenberg, K., Bohnenberger, H., Lenz, C., Henze, S.,

955 Stauske, M., Salinas, G., Zimmermann, W.H., et al. (2018). Deep phenotyping of human induced

956 pluripotent stem cell-derived atrial and ventricular cardiomyocytes. *JCI Insight* 3.

957 10.1172/jci.insight.99941.

958 Driscoll, D.J., Offord, K.P., Feldt, R.H., Schaff, H.V., Puga, F.J., and Danielson, G.K. (1992). Five-

959 to fifteen-year follow-up after Fontan operation. *Circulation* 85, 469-496. 10.1161/01.cir.85.2.469.

960 Dubois, N.C., Craft, A.M., Sharma, P., Elliott, D.A., Stanley, E.G., Elefanty, A.G., Gramolini, A.,

961 and Keller, G. (2011). SIRPA is a specific cell-surface marker for isolating cardiomyocytes derived

962 from human pluripotent stem cells. *Nat Biotechnol* 29, 1011-U1082. 10.1038/nbt.2005.

963 Elia, A.E., Lalli, S., Monsurro, M.R., Sagnelli, A., Taiello, A.C., Reggiori, B., La Bella, V.,

964 Tedeschi, G., and Albanese, A. (2016). Tauroursodeoxycholic acid in the treatment of patients with

965 amyotrophic lateral sclerosis. *Eur J Neurol* 23, 45-52. 10.1111/ene.12664.

966 Feinstein, J.A., Benson, D.W., Dubin, A.M., Cohen, M.S., Maxey, D.M., Mahle, W.T., Pahl, E.,

967 Villafane, J., Bhatt, A.B., Peng, L.F., et al. (2012). Hypoplastic left heart syndrome: current

968 considerations and expectations. *J Am Coll Cardiol* 59, S1-42. 10.1016/j.jacc.2011.09.022.

969 Fortini, P., Ferretti, C., Iorio, E., Cagnin, M., Garribba, L., Pietraforte, D., Falchi, M., Pascucci, B.,

970 Baccarini, S., Morani, F., et al. (2016a). The fine tuning of metabolism, autophagy and

971 differentiation during in vitro myogenesis. *Cell Death Dis* 7, e2168. 10.1038/cddis.2016.50.

972 Fortini, P., Iorio, E., Dogliotti, E., and Isidoro, C. (2016b). Coordinated Metabolic Changes and

973 Modulation of Autophagy during Myogenesis. *Front Physiol* 7, 237. 10.3389/fphys.2016.00237.

974 funakoshi, s., , M.N., , C.O., , K.M., , T.K., , S.Y., , A.W., and , Y.Y. (2018). Abstract 16184: Single

975 Cell RNA Sequencing Reveals Dynamic and Heterogeneous Changes of Transcriptome During

976 Cardiac Differentiation in vitro. *Circulation* 2014;130:A16184.

977 Fusaki, N., Ban, H., Nishiyama, A., Saeki, K., and Hasegawa, M. (2009). Efficient induction of

978 transgene-free human pluripotent stem cells using a vector based on Sendai virus, an RNA virus

979 that does not integrate into the host genome. *P Jpn Acad B-Phys* 85, 348-362. 10.2183/pjab.85.348.

980 Gaber, N., Gagliardi, M., Patel, P., Kinnear, C., Zhang, C., Chitayat, D., Shannon, P., Jaeggi, E.,

981 Tabori, U., Keller, G., and Mital, S. (2013). Fetal reprogramming and senescence in hypoplastic

982 left heart syndrome and in human pluripotent stem cells during cardiac differentiation. *Am J Pathol*

983 183, 720-734. 10.1016/j.ajpath.2013.05.022.

984 Galie, N., Ghofrani, H.A., Torbicki, A., Barst, R.J., Rubin, L.J., Badesch, D., Fleming, T., Parpia,

985 T., Burgess, G., Branzi, A., et al. (2005). Sildenafil citrate therapy for pulmonary arterial

986 hypertension. *N Engl J Med* 353, 2148-2157. 10.1056/NEJMoa050010.

987 Galmiche, L., Serre, V., Beinat, M., Assouline, Z., Lebre, A.S., Chretien, D., Nietschke, P., Benes,

988 V., Boddaert, N., Sidi, D., et al. (2011). Exome sequencing identifies MRPL3 mutation in

989 mitochondrial cardiomyopathy. *Hum Mutat* 32, 1225-1231. 10.1002/humu.21562.

990 Ganapathiraju, M.K., Thahir, M., Handen, A., Sarkar, S.N., Sweet, R.A., Nimgaonkar, V.L.,

991 Loscher, C.E., Bauer, E.M., and Chaparala, S. (2016). Schizophrenia interactome with 504 novel

992 protein-protein interactions. *Npj Schizophr* 2. UNSP 16012

993 10.1038/npjSchz.2016.12.

994 Garcia, A.M., Beatty, J.T., and Nakano, S.J. (2020). Heart failure in single right ventricle

995 congenital heart disease: physiological and molecular considerations. *Am J Physiol Heart Circ*

- 996 *Physiol* 318, H947-H965. 10.1152/ajpheart.00518.2019.
- 997 Gentles, T.L., Gauvreau, K., Mayer, J.E., Jr., Fishberger, S.B., Burnett, J., Colan, S.D., Newburger,
998 J.W., and Wernovsky, G. (1997). Functional outcome after the Fontan operation: factors
999 influencing late morbidity. *J Thorac Cardiovasc Surg* 114, 392-403; discussion 404-395.
1000 10.1016/s0022-5223(97)70184-3.
- 1001 Guglin, M., Rajagopalan, N., Anaya, P., and Charnigo, R. (2016). Sildenafil in heart failure with
1002 reactive pulmonary hypertension (Sildenafil HF) clinical trial (rationale and design). *Pulm Circ* 6,
1003 161-167. 10.1086/685548.
- 1004 Guimaraes-Camboa, N., Stowe, J., Aneas, I., Sakabe, N., Cattaneo, P., Henderson, L., Kilberg,
1005 M.S., Johnson, R.S., Chen, J., McCulloch, A.D., et al. (2015). HIF1alpha Represses Cell Stress
1006 Pathways to Allow Proliferation of Hypoxic Fetal Cardiomyocytes. *Dev Cell* 33, 507-521.
1007 10.1016/j.devcel.2015.04.021.
- 1008 Heallen, T., Morikawa, Y., Leach, J., Tao, G., Willerson, J.T., Johnson, R.L., and Martin, J.F. (2013).
1009 Hippo signaling impedes adult heart regeneration. *Development* 140, 4683-4690.
1010 10.1242/dev.102798.
- 1011 Hom, J.R., Quintanilla, R.A., Hoffman, D.L., de Mesy Bentley, K.L., Molkentin, J.D., Sheu, S.S.,
1012 and Porter, G.A., Jr. (2011). The permeability transition pore controls cardiac mitochondrial
1013 maturation and myocyte differentiation. *Dev Cell* 21, 469-478. 10.1016/j.devcel.2011.08.008.
- 1014 Hrstka, S.C.L., Li, X., Nelson, T.J., and Pipeline, W.P.G. (2017). NOTCH1-Dependent Nitric
1015 Oxide Signaling Deficiency in Hypoplastic Left Heart Syndrome Revealed Through Patient-
1016 Specific Phenotypes Detected in Bioengineered Cardiogenesis. *Stem Cells* 35, 1106-1119.
1017 10.1002/stem.2582.
- 1018 Hsu, D.T., Zak, V., Mahony, L., Sleeper, L.A., Atz, A.M., Levine, J.C., Barker, P.C., Ravishankar,
1019 C., McCrindle, B.W., Williams, R.V., et al. (2010). Enalapril in infants with single ventricle: results
1020 of a multicenter randomized trial. *Circulation* 122, 333-340.
1021 10.1161/CIRCULATIONAHA.109.927988.
- 1022 Huang, S., Wang, X., Wu, X., Yu, J., Li, J., Huang, X., Zhu, C., and Ge, H. (2018). Yap regulates
1023 mitochondrial structural remodeling during myoblast differentiation. *Am J Physiol Cell Physiol*
1024 315, C474-C484. 10.1152/ajpcell.00112.2018.
- 1025 Itoh, K., Wakabayashi, N., Katoh, Y., Ishii, T., Igarashi, K., Engel, J.D., and Yamamoto, M. (1999).
1026 Keap1 represses nuclear activation of antioxidant responsive elements by Nrf2 through binding to
1027 the amino-terminal Neh2 domain. *Genes Dev* 13, 76-86. 10.1101/gad.13.1.76.
- 1028 Jiang, Y., Habibollah, S., Tilgner, K., Collin, J., Barta, T., Al-Aama, J.Y., Tesarov, L., Hussain, R.,
1029 Trafford, A.W., Kirkwood, G., et al. (2014a). An Induced Pluripotent Stem Cell Model of
1030 Hypoplastic Left Heart Syndrome (HLHS) Reveals Multiple Expression and Functional
1031 Differences in HLHS-Derived Cardiac Myocytes. *Stem Cells Transl Med* 3, 416-423.
1032 10.5966/sctm.2013-0105.
- 1033 Jiang, Y., Habibollah, S., Tilgner, K., Collin, J., Barta, T., Al-Aama, J.Y., Tesarov, L., Hussain, R.,
1034 Trafford, A.W., Kirkwood, G., et al. (2014b). An induced pluripotent stem cell model of
1035 hypoplastic left heart syndrome (HLHS) reveals multiple expression and functional differences in
1036 HLHS-derived cardiac myocytes. *Stem Cells Transl Med* 3, 416-423. 10.5966/sctm.2013-0105.
- 1037 Kanehisa, M., Araki, M., Goto, S., Hattori, M., Hirakawa, M., Itoh, M., Katayama, T., Kawashima,
1038 S., Okuda, S., Tokimatsu, T., and Yamanishi, Y. (2008). KEGG for linking genomes to life and the
1039 environment. *Nucleic Acids Res* 36, D480-D484. 10.1093/nar/gkm882.
- 1040 Karczewski, K.J., Francioli, L.C., Tiao, G., Cummings, B.B., Alfoldi, J., Wang, Q., Collins, R.L.,
1041 Laricchia, K.M., Ganna, A., Birnbaum, D.P., et al. (2020). The mutational constraint spectrum

1042 quantified from variation in 141,456 humans. *Nature* 581, 434-443. 10.1038/s41586-020-2308-7.
1043 Kobayashi, J., Yoshida, M., Tarui, S., Hirata, M., Nagai, Y., Kasahara, S., Naruse, K., Ito, H., Sano,
1044 S., and Oh, H. (2014). Directed differentiation of patient-specific induced pluripotent stem cells
1045 identifies the transcriptional repression and epigenetic modification of NKX2-5, HAND1, and
1046 NOTCH1 in hypoplastic left heart syndrome. *PLoS One* 9, e102796.
1047 10.1371/journal.pone.0102796.
1048 Liu, X., Wu, C., Li, C., and Boerwinkle, E. (2016). dbNSFP v3.0: A One-Stop Database of
1049 Functional Predictions and Annotations for Human Nonsynonymous and Splice-Site SNVs. *Hum*
1050 *Mutat* 37, 235-241. 10.1002/humu.22932.
1051 Liu, X., Yagi, H., Saeed, S., Bais, A.S., Gabriel, G.C., Chen, Z., Peterson, K.A., Li, Y., Schwartz,
1052 M.C., Reynolds, W.T., et al. (2017). The complex genetics of hypoplastic left heart syndrome. *Nat*
1053 *Genet* 49, 1152-1159. 10.1038/ng.3870.
1054 Marin-Garcia, J., and Akhmedov, A.T. (2016). Mitochondrial dynamics and cell death in heart
1055 failure. *Heart Fail Rev* 21, 123-136. 10.1007/s10741-016-9530-2.
1056 Martel, C., Huynh le, H., Garnier, A., Ventura-Clapier, R., and Brenner, C. (2012). Inhibition of
1057 the Mitochondrial Permeability Transition for Cytoprotection: Direct versus Indirect Mechanisms.
1058 *Biochem Res Int* 2012, 213403. 10.1155/2012/213403.
1059 McCarthy, D.J., Campbell, K.R., Lun, A.T.L., and Wills, Q.F. (2017). Scater: pre-processing,
1060 quality control, normalization and visualization of single-cell RNA-seq data in R. *Bioinformatics*
1061 33, 1179-1186. 10.1093/bioinformatics/btw777.
1062 McKenna, A., Hanna, M., Banks, E., Sivachenko, A., Cibulskis, K., Kernytsky, A., Garimella, K.,
1063 Altshuler, D., Gabriel, S., Daly, M., and DePristo, M.A. (2010). The Genome Analysis Toolkit: a
1064 MapReduce framework for analyzing next-generation DNA sequencing data. *Genome Res* 20,
1065 1297-1303. 10.1101/gr.107524.110.
1066 Meng, Z., Moroishi, T., and Guan, K.L. (2016). Mechanisms of Hippo pathway regulation. *Genes*
1067 *Dev* 30, 1-17. 10.1101/gad.274027.115.
1068 Miao, Y., Tian, L., Martin, M., Paige, S.L., Galdos, F.X., Li, J., Klein, A., Zhang, H., Ma, N., Wei,
1069 Y., et al. (2020). Intrinsic Endocardial Defects Contribute to Hypoplastic Left Heart Syndrome.
1070 *Cell Stem Cell* 27, 574-589 e578. 10.1016/j.stem.2020.07.015.
1071 Mills, R.J., Titmarsh, D.M., Koenig, X., Parker, B.L., Ryall, J.G., Quaife-Ryan, G.A., Voges, H.K.,
1072 Hodson, M.P., Ferguson, C., Drowley, L., et al. (2017). Functional screening in human cardiac
1073 organoids reveals a metabolic mechanism for cardiomyocyte cell cycle arrest. *Proc Natl Acad Sci*
1074 *U S A* 114, E8372-E8381. 10.1073/pnas.1707316114.
1075 Myung, S.K., Ju, W., Cho, B., Oh, S.W., Park, S.M., Koo, B.K., Park, B.J., and Korean Meta-
1076 Analysis Study, G. (2013). Efficacy of vitamin and antioxidant supplements in prevention of
1077 cardiovascular disease: systematic review and meta-analysis of randomised controlled trials. *BMJ*
1078 346, f10. 10.1136/bmj.f10.
1079 Nakano, H., Minami, I., Braas, D., Pappoe, H., Wu, X., Sagadevan, A., Vergnes, L., Fu, K.,
1080 Morselli, M., Dunham, C., et al. (2017). Glucose inhibits cardiac muscle maturation through
1081 nucleotide biosynthesis. *Elife* 6. 10.7554/eLife.29330.
1082 Okita, K., Matsumura, Y., Sato, Y., Okada, A., Morizane, A., Okamoto, S., Hong, H., Nakagawa,
1083 M., Tanabe, K., Tezuka, K., et al. (2011). A more efficient method to generate integration-free
1084 human iPS cells. *Nat Methods* 8, 409-U452. 10.1038/Nmeth.1591.
1085 Oster, M.E., Lee, K.A., Honein, M.A., Riehle-Colarusso, T., Shin, M., and Correa, A. (2013).
1086 Temporal trends in survival among infants with critical congenital heart defects. *Pediatrics* 131,
1087 e1502-1508. 10.1542/peds.2012-3435.

1088 Pagliarini, D.J., Calvo, S.E., Chang, B., Sheth, S.A., Vafai, S.B., Ong, S.E., Walford, G.A., Sugiana,
1089 C., Boneh, A., Chen, W.K., et al. (2008). A mitochondrial protein compendium elucidates complex
1090 I disease biology. *Cell* 134, 112-123. 10.1016/j.cell.2008.06.016.
1091 Paige, S.L., Galdos, F.X., Lee, S., Chin, E.T., Ranjbarvaziri, S., Feyen, D.A.M., Darsha, A.K., Xu,
1092 S., Ryan, J.A., Beck, A.L., et al. (2020). Patient-Specific Induced Pluripotent Stem Cells Implicate
1093 Intrinsic Impaired Contractility in Hypoplastic Left Heart Syndrome. *Circulation* 142, 1605-1608.
1094 10.1161/CIRCULATIONAHA.119.045317.
1095 Perrelli, M.G., Pagliaro, P., and Penna, C. (2011). Ischemia/reperfusion injury and cardioprotective
1096 mechanisms: Role of mitochondria and reactive oxygen species. *World J Cardiol* 3, 186-200.
1097 10.4330/wjc.v3.i6.186.
1098 Pile, L.A., Spellman, P.T., Katzenberger, R.J., and Wassarman, D.A. (2003). The SIN3 deacetylase
1099 complex represses genes encoding mitochondrial proteins: implications for the regulation of
1100 energy metabolism. *J Biol Chem* 278, 37840-37848. 10.1074/jbc.M305996200.
1101 Prabhu, L.V., Rai, R., Ranade, A.V., Kini, H., Krishnamurthy, A., and Bernhardt, K.L. (2013).
1102 Effect of sildenafil-induced nitric oxide on the histomorphology of cardiomyocytes in male rats.
1103 *Int J Appl Basic Med Res* 3, 84-87. 10.4103/2229-516X.117056.
1104 Prasad, T.S.K., Goel, R., Kandasamy, K., Keerthikumar, S., Kumar, S., Mathivanan, S.,
1105 Telikicherla, D., Raju, R., Shafreen, B., Venugopal, A., et al. (2009). Human Protein Reference
1106 Database-2009 update. *Nucleic Acids Res* 37, D767-D772. 10.1093/nar/gkn892.
1107 Rooney, J.P., Ryde, I.T., Sanders, L.H., Howlett, E.H., Colton, M.D., Germ, K.E., Mayer, G.D.,
1108 Greenamyre, J.T., and Meyer, J.N. (2015). PCR based determination of mitochondrial DNA copy
1109 number in multiple species. *Methods Mol Biol* 1241, 23-38. 10.1007/978-1-4939-1875-1_3.
1110 Schiattarella, G.G., Altamirano, F., Tong, D., French, K.M., Villalobos, E., Kim, S.Y., Luo, X.,
1111 Jiang, N., May, H.I., Wang, Z.V., et al. (2019). Nitrosative stress drives heart failure with preserved
1112 ejection fraction. *Nature* 568, 351-356. 10.1038/s41586-019-1100-z.
1113 Schuster, J., Halvardson, J., Pilar Lorenzo, L., Ameer, A., Sobol, M., Raykova, D., Anneren, G.,
1114 Feuk, L., and Dahl, N. (2015). Transcriptome Profiling Reveals Degree of Variability in Induced
1115 Pluripotent Stem Cell Lines: Impact for Human Disease Modeling. *Cell Reprogram* 17, 327-337.
1116 10.1089/cell.2015.0009.
1117 Shaddy, R.E., Boucek, M.M., Hsu, D.T., Boucek, R.J., Canter, C.E., Mahony, L., Ross, R.D., Pahl,
1118 E., Blume, E.D., Dodd, D.A., et al. (2007). Carvedilol for children and adolescents with heart
1119 failure: a randomized controlled trial. *JAMA* 298, 1171-1179. 10.1001/jama.298.10.1171.
1120 Stark, C., Breitkreutz, B.J., Chatr-Aryamontri, A., Boucher, L., Oughtred, R., Livstone, M.S.,
1121 Nixon, J., Van Auken, K., Wang, X., Shi, X., et al. (2011). The BioGRID Interaction Database:
1122 2011 update. *Nucleic Acids Res* 39, D698-704. 10.1093/nar/gkq1116.
1123 Stuart, T., Butler, A., Hoffman, P., Hafemeister, C., Papalexi, E., Mauck, W.M., 3rd, Hao, Y.,
1124 Stoeckius, M., Smibert, P., and Satija, R. (2019). Comprehensive Integration of Single-Cell Data.
1125 *Cell* 177, 1888-1902 e1821. 10.1016/j.cell.2019.05.031.
1126 Tan, Y., and Cahan, P. (2019). SingleCellNet: A Computational Tool to Classify Single Cell RNA-
1127 Seq Data Across Platforms and Across Species. *Cell Syst* 9, 207-213 e202.
1128 10.1016/j.cels.2019.06.004.
1129 Tao, G., Kahr, P.C., Morikawa, Y., Zhang, M., Rahmani, M., Heallen, T.R., Li, L., Sun, Z., Olson,
1130 E.N., Amendt, B.A., and Martin, J.F. (2016). Pitx2 promotes heart repair by activating the
1131 antioxidant response after cardiac injury. *Nature* 534, 119-123. 10.1038/nature17959.
1132 Tsutsui, H., Kinugawa, S., and Matsushima, S. (2011). Oxidative stress and heart failure. *Am J*
1133 *Physiol Heart Circ Physiol* 301, H2181-2190. 10.1152/ajpheart.00554.2011.

1134 Tweddell, J.S., Hoffman, G.M., Mussatto, K.A., Fedderly, R.T., Berger, S., Jaquiss, R.D.,
1135 Ghanayem, N.S., Frisbee, S.J., and Litwin, S.B. (2002). Improved survival of patients undergoing
1136 palliation of hypoplastic left heart syndrome: lessons learned from 115 consecutive patients.
1137 *Circulation* *106*, I82-89.

1138 Ventura-Clapier, R., Garnier, A., Veksler, V., and Joubert, F. (2011). Bioenergetics of the failing
1139 heart. *Bba-Mol Cell Res* *1813*, 1360-1372. 10.1016/j.bbamcr.2010.09.006.

1140 von Gise, A., Lin, Z., Schlegelmilch, K., Honor, L.B., Pan, G.M., Buck, J.N., Ma, Q., Ishiwata, T.,
1141 Zhou, B., Camargo, F.D., and Pu, W.T. (2012). YAP1, the nuclear target of Hippo signaling,
1142 stimulates heart growth through cardiomyocyte proliferation but not hypertrophy. *Proc Natl Acad*
1143 *Sci U S A* *109*, 2394-2399. 10.1073/pnas.1116136109.

1144 Wang, K., Li, M., and Hakonarson, H. (2010). ANNOVAR: functional annotation of genetic
1145 variants from high-throughput sequencing data. *Nucleic Acids Res* *38*, e164. 10.1093/nar/gkq603.

1146 Wolf, F.A., Angerer, P., and Theis, F.J. (2018). SCANPY: large-scale single-cell gene expression
1147 data analysis. *Genome Biol* *19*, 15. 10.1186/s13059-017-1382-0.

1148 Xinxu Xu, T.T., Jiuann-Huey Ivy Lin, Phillips Adams, Xiaoqin Liu, Feinstein Timothy N , Omar
1149 Khalifa, George A Porter Jr, Sruti S. Shiva, Cecilia W. Lo (2018). Intrinsic Cardiomyocyte
1150 Mitochondrial Defects Underlie Cardiac Dysfunction and Heart Failure Risk Associated with
1151 Hypoplastic Left Heart Syndrome. *Circulation*. *2018;138:A15746*.

1152 Xu, X., Wang, Q., Long, Y., Zhang, R., Wei, X., Xing, M., Gu, H., and Xie, X. (2013). Stress-
1153 mediated p38 activation promotes somatic cell reprogramming. *Cell Res* *23*, 131-141.
1154 10.1038/cr.2012.143.

1155 Ye, Y., Li, J., and Yuan, Z. (2013). Effect of antioxidant vitamin supplementation on cardiovascular
1156 outcomes: a meta-analysis of randomized controlled trials. *PLoS One* *8*, e56803.
1157 10.1371/journal.pone.0056803.

1158 Zhou, Q., Li, L., Zhao, B., and Guan, K.L. (2015). The hippo pathway in heart development,
1159 regeneration, and diseases. *Circ Res* *116*, 1431-1447. 10.1161/CIRCRESAHA.116.303311.

1160

Fig1

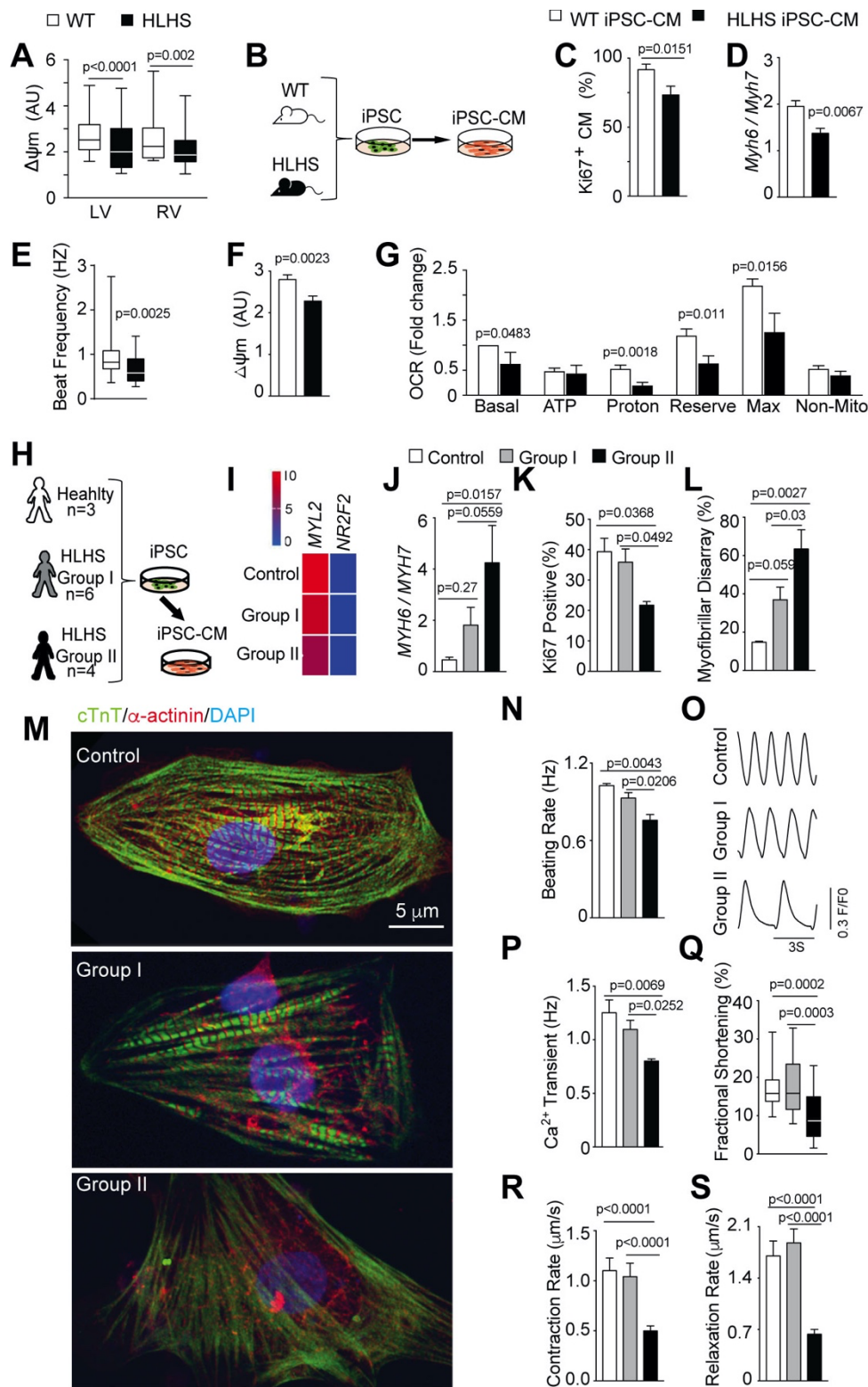


Fig2

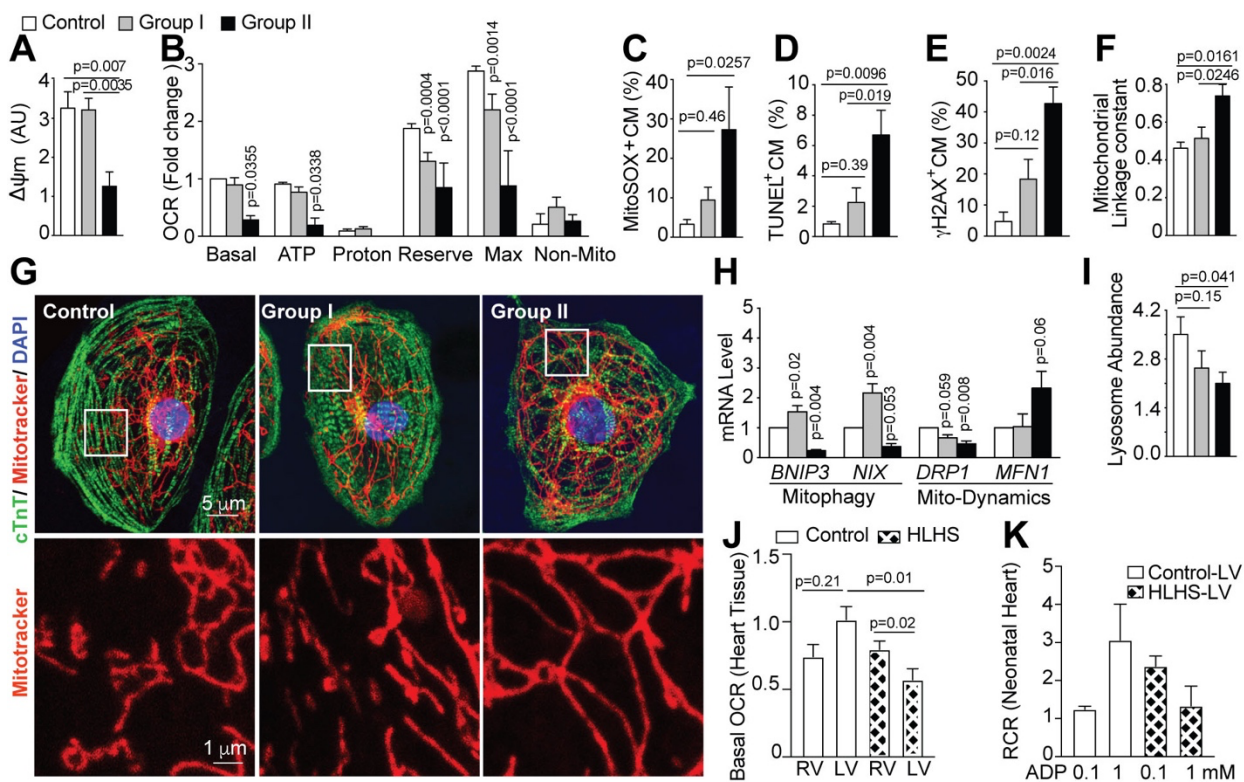


Fig3

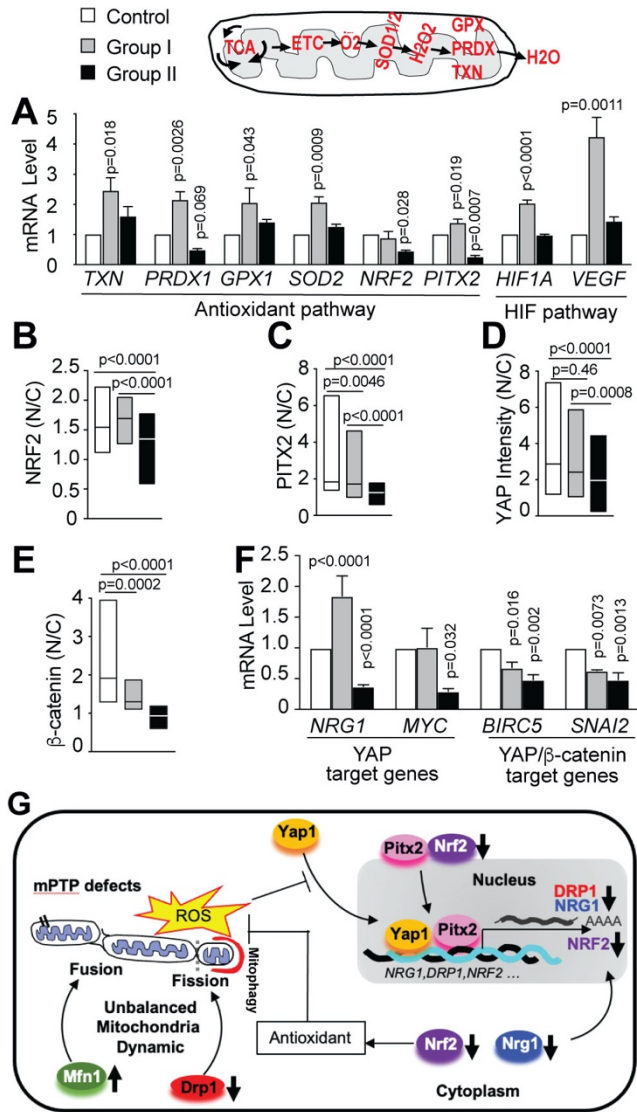


Fig4

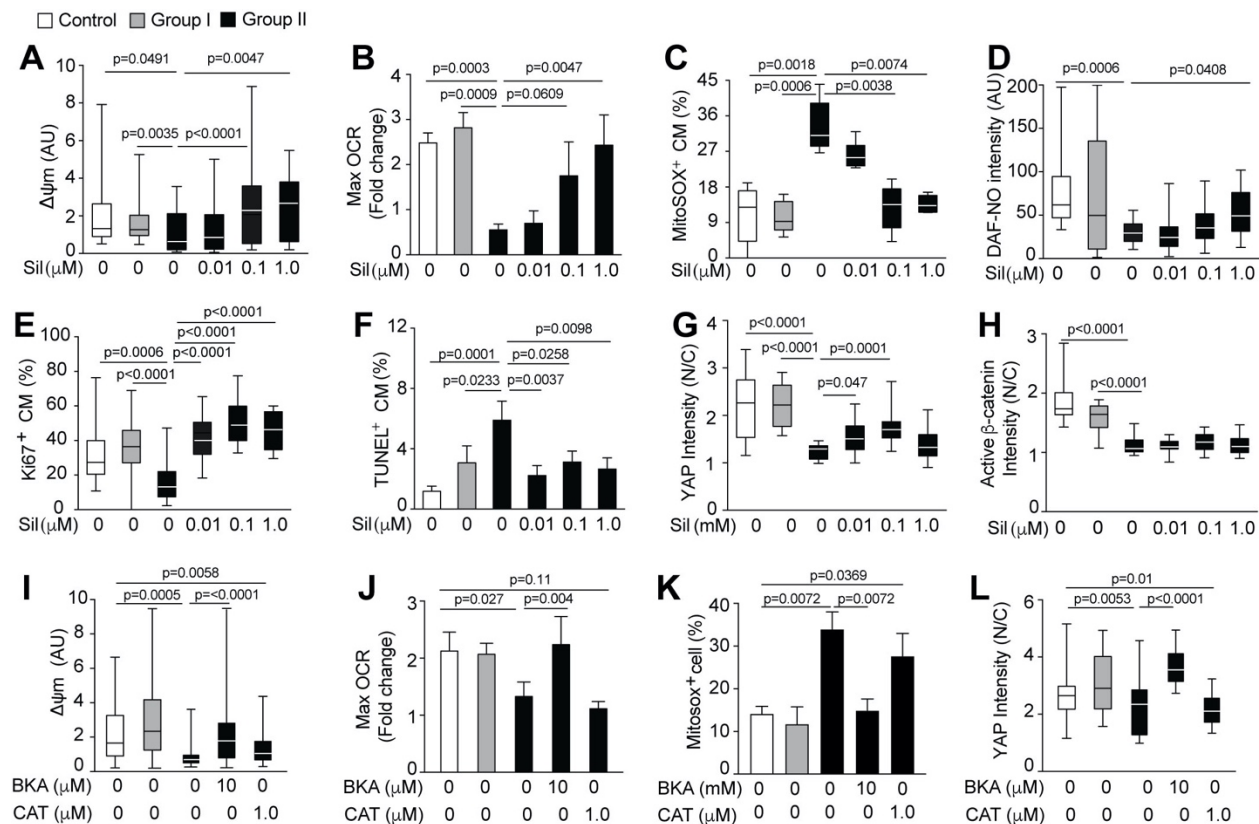


Fig5

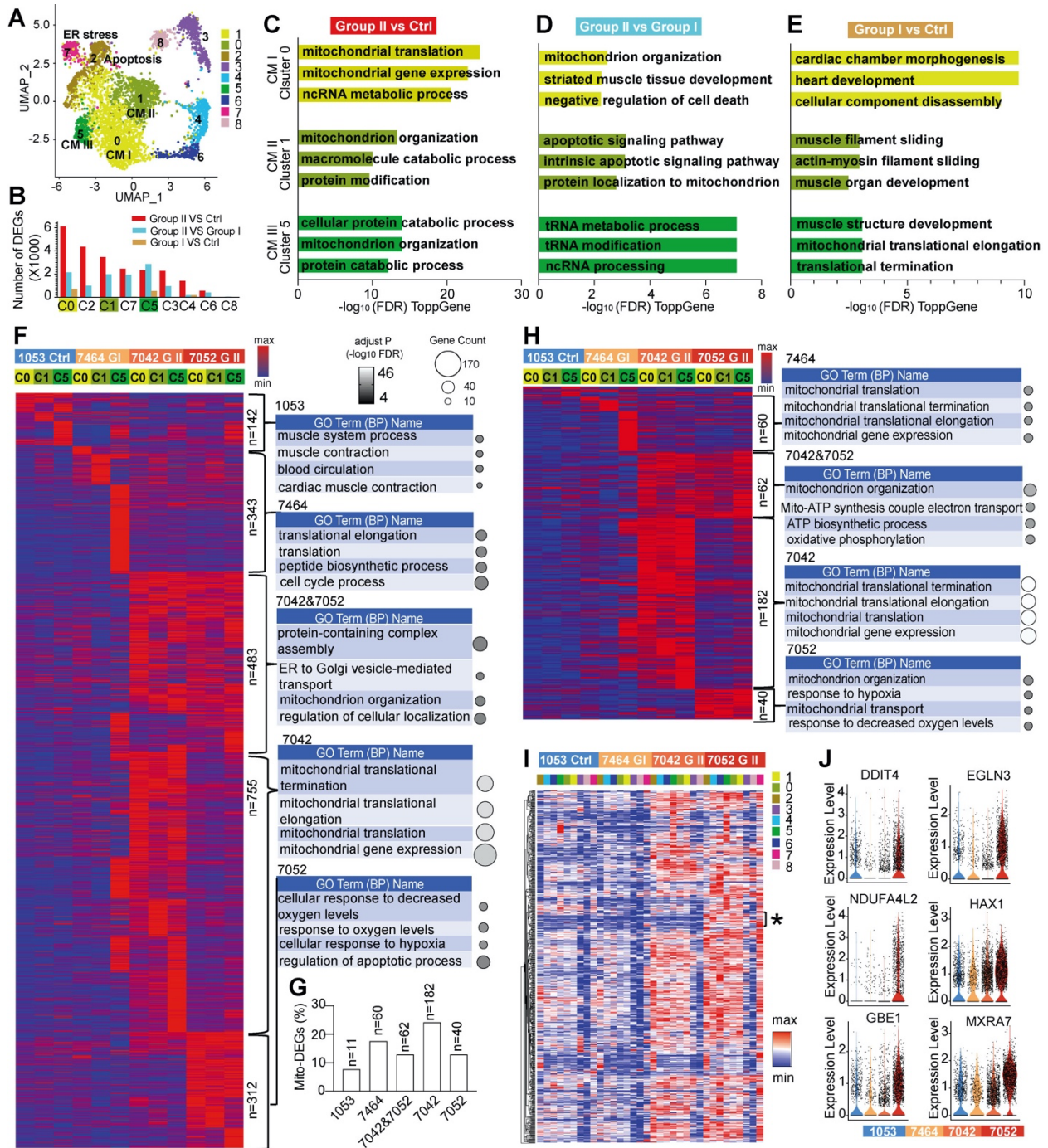


Fig6

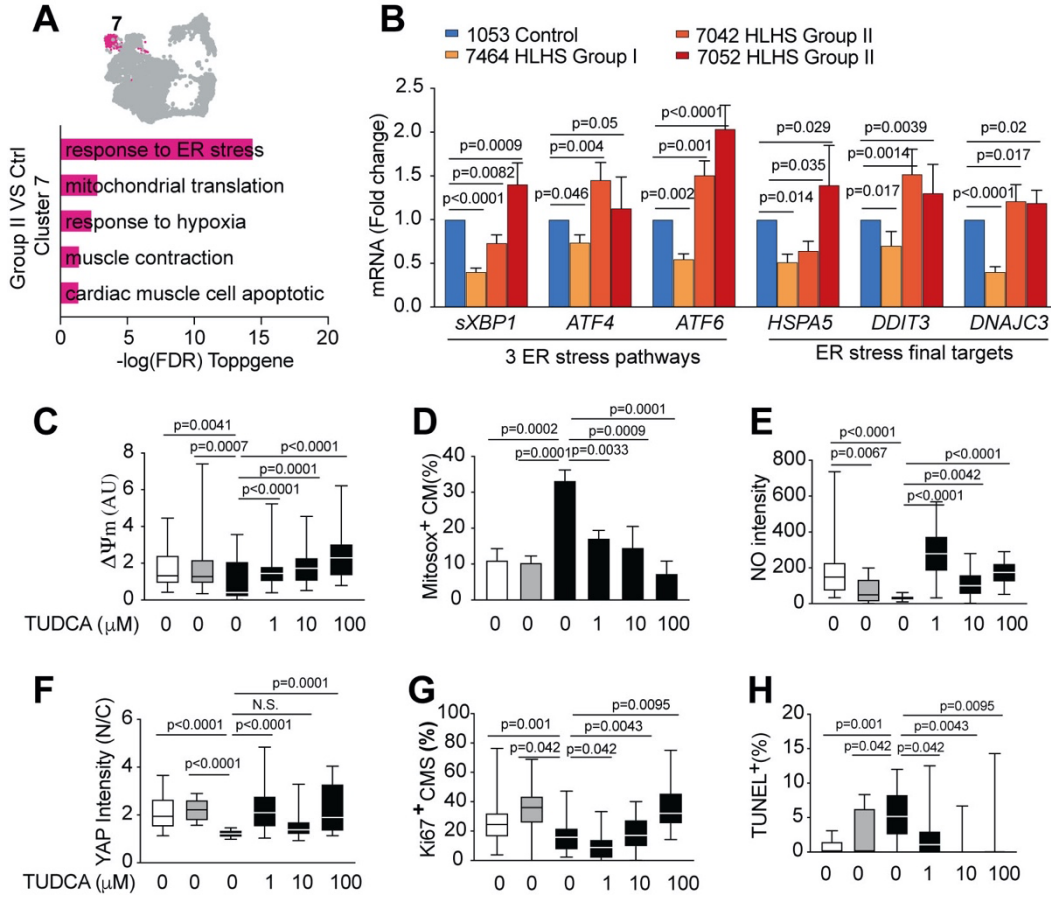


Fig7

